2017

# An Investigation on the Stress Intensity Factor of Surface Micro-cracks

Sirisha Divya Arli
*Wright State University*

# AN INVESTIGATION ON THE STRESS INTENSITY FACTOR OF SURFACE MICRO-CRACKS

A thesis submitted in partial fulfillment of
the requirements for the degree of Master of
Science in Mechanical Engineering

By

SIRISHA DIVYA ARLI

B.Tech, Jawaharlal Nehru Technological University, 2004
M. Tech, Manipal Institute of Techonology, 2006

2017

Wright State University

WRIGHT STATE UNIVERSITY

GRADUATE SCHOOL

03/24/2017

I HEREBY RECOMMEND THAT THE THESIS PREPARED UNDER MY SUPERVISION BY Sirisha Divya Arli ENTITLED An Investigation on the Stress Intensity Factor of Surface Micro-cracks BE ACCEPTED IN PARTIAL FULFILLMENT OF THE REQUIREMENTS FOR THE DEGREE OF Master of Science in Mechanical Engineering.

_____

Sheng Li, Ph.D.
Thesis Director

_____

Joseph C. Slater, Ph.D., PE
Chair, Department of MME

Committee on Final Examination

_____

Sheng Li, Ph.D.

_____

Ha-Rok Bae, Ph.D.

_____

Ahsan Mian, Ph.D.

_____

Robert E. W. Fyffe, Ph.D.
Vice President for Research and
Dean of the Graduate School

## ABSTRACT

Arli, Sirisha Divya. M.S.M.E., Department of Mechanical and Materials Engineering, Wright State University, 2017. *An Investigation on the Stress Intensity Factor of Surface Micro-cracks.*

The contact fatigue failure in the form of micro or macro-scale pitting is an important failure mode for rolling mechanical elements, such as bearings and gears that are widely used in the automotive, aerospace and wind turbine fields. The micro-pitting process in some cases, gradually removes the surface material through fatigue wear, altering the geometry of the contact surfaces to alleviate the contact pressure decelerating the continued pitting rate. The propagation of the micro-cracks in other cases, goes deep into the material along a shallow angle, turns parallel to the surface at a certain depth, where the maximum shear or material voids or impurities take place, and lastly turns back to the surface, forming macro-sized pits changing the geometry of the contact surface, resulting in large vibration and dynamic behavior of the mechanical components. The propagation of a crack is tightly related to the stress concentration in the vicinity of the crack tip. This study investigates the Stress Intensity Factor (SIF) of Surface Micro-cracks under Hertzian and Sinusoidal pressure distributions considering the effects of surface friction imitating the smooth and rough contact surfaces. The finite element approach is used establish the computational model and to examine the impacts of the crack length, the crack orientation, the surface friction and different type of loading on SIF.

## TABLE OF CONTENTS

## LIST OF FIGURES

## LIST OF TABLES

**ACKNOWLEDGEMENTS**

To my life-educator, my late mother, Gayathri: because I owe it all to you. Thank you.

I would like to express my sincere gratitude to my advisor, Dr. Sheng Li for the continuous support of my thesis, for his patience, motivation, enthusiasm, immense knowledge and funding. His guidance helped me in all the time of research and writing of this thesis. I could not have imagined having a better advisor and mentor for my master's thesis. I am also thankful for being the excellent example he has provided as a researcher and teacher.

Besides my advisor, I would like to thank the rest of my thesis committee: Dr. Ha-Rok Bae and Dr. Ahsan Mian, for their encouragement and insightful comments. Special thanks to Gregory Wilt and Mike Vanhorn for all the help whenever I needed.

I am grateful to my sister and father, Deepthi and Narayan, who have provided me through moral and emotional support in my life.

A very special gratitude to my mentors in professional career, Puppala Krishna Tulasi and Sai Krishna Danda.

With a special mention to my bestie, Anusha for always guiding and challenging my work. Thierry, Shravan and Ranjith for their support, love, patience and unending debates mostly on everything.

Lastly, I am forever grateful to my beloved husband, Krishna without whom this would not have been possible, for loving, supporting and continuously pushing me to do and be my best always.

*Dedicated to my parents and Husband*

# CHAPTER 1

# INTRODUCTION

## 1.1 Background and Motivation

The contact fatigue failure in the form of micro or macro-scale pitting has become an important failure mode for rolling mechanical elements, such as bearings and gears that are widely used in the automotive, aerospace and wind turbine fields. Under certain circumstances, the micro-pitting process gradually removes the surface material through fatigue wear, altering the geometry of the contact surfaces to alleviate the contact pressure and therefore decelerate the continued pitting rate. Under this scenario, the machine element can usually operate for an elongated period of time without the need for replacement. Another commonly observed phenomenon is that the propagation of the micro-cracks goes deep into the material along a shallow angle, turns parallel to the surface at a certain depth, where the maximum shear or material voids or impurities take place, and lastly turns back to the surface, forming macro-sized pits. The macro-pit significantly changes the geometry of the contact surface, resulting in large vibration and dynamic behavior of the mechanical components. Especially under the high-speed application

condition, the dynamic response can introduce large dynamic contact force and greatly accelerate the further growth of the pit, quickly destroying the component.

The propagation of a crack is tightly related to the stress concentration in the vicinity of the crack tip. An approach to mathematically relate the crack propagation life to the crack propagation length is through the law proposed by Paris and Erdogan [1] as

$$\frac{da}{dN} = C\Delta K_e^m \tag{1.1}$$

where $a$ is the crack length, $N$ is the number of loading cycles, and $C$ and $m$ are material specific parameters, requiring the experimental determination. In addition, $\Delta K_e$ in Equation (1.1) represents the range of the effective stress intensity factor (SIF) that is a combination of the mode I SIF range, $\Delta K_I$, and the mode II SIF range, $\Delta K_{II}$, in the form of

$$\Delta K_e^4 = \Delta K_I^4 + 8\Delta K_{II}^4 \tag{1.2}$$

In view of the above formulation, the stress intensity factor plays an important role in the process of the crack propagation. Therefore, this study investigates the behavior of the stress intensity factor of micro-cracks.

In recent years, the surface nucleated fatigue cracks have become much more frequent in comparison to the subsurface nucleated fatigue cracks. The reasons include several: (i) The materials nowadays are much cleaner in comparing to the past, and the subsurface formed cracks due to impurities and voids inside the material become less likely; (ii) The case hardening technique has been widely implemented to reinforce the

fatigue strength of the surface layer of the mechanical component, covering the depth where subsurface cracks are usually nucleated; (iii) The presence of the surface roughness profiles due to the finishing machining process leads to significant contact pressure peaks and consequently near surface stress concentrations [2-11]; (iv) The wear particles in the lubricant act as stress raisers within the contact zone. This study therefore addresses the more frequently occurred surface nucleated cracks.

Although many rolling mechanical elements commonly operate under the lubricated condition, the lubrication does not significantly alter the contact pressure distribution under the smooth surface condition. As such, a Hertzian contact pressure distribution is employed in this work. The surface friction is applied by introducing a constant friction coefficient throughout the contact zone. To simulate the rough surface condition, a Sinusoidal contact pressure distribution is implemented. The objective of this study is to numerically evaluate the stress intensity factor (SIF) of a micro-crack under the line contact condition, examining the impacts of the crack length, the crack orientation, the surface friction, and different loading type (Hertzian pressure distribution for smooth surface condition, and Sinusoidal pressure distribution for rough surface condition) on the SIF behavior as the surface loadings move across the crack. The finite element approach is used in the study. The obtained SIF data set can be used to construct an easy-to-use formula through the general linear regression technique, expressing the SIF as a function of the interested crack and contact parameters and facilitating the evaluation of the crack propagation behavior.

## 1.2 Literature Review

Miller et al. [12] investigated the propagation mechanics of both surface and subsurface nucleated cracks under cyclic contact loading. Most surface breaking cracks were observed to arrest when reaching the size of 10-20 μm, forming micro-pits on the surface. Some of these cracks, however, propagated further to produce macro-pits. This continued propagation was attributed to the presence of the near surface inclusions, which raised the local stress intensity factor range. Through the inclusions, the micro-cracks grew and reached macro-scale dimensions. To quantitatively link the crack propagation life to the stress intensity factor within wide ranges of the crack size (short and long) and the crack growth rate (slow and fast), the empirical McEvily-Foreman relationship was adopted. In the analysis, the surface asperity contact pressure was considered, while the EHL fluid effects in crack growth was excluded. Bower [13] modeled the growth of long cracks due to the movement of the trapped fluid towards the crack tips. The initial crack length was assumed to be half of the Hertzian width to allow the applicability of the linear elastic fracture mechanics. In this study, the mode II (shear mode) crack propagation was also discussed. It was shown: (i) the mode II stress intensity factor is sensitive to the direction of the surface shear in the way that negative sliding leads to larger stress intensities; and (ii) The mode II stress intensity factor is also sensitive to the crack face friction. When the friction coefficient is larger than 0.2, the resultant stress intensity factor can hardly promote any crack prorogation.

Bogdanski [14, 15] included the description of the fluid flow within the crack in the long crack growth modeling. The stress intensity factors were evaluated using the finite

element (FE) approach. For the reduction in the computational efforts in stress intensity evaluation, Bogdanski and Trajer [16] proposed a dimensionless approach for the FE modeling. Take one step further, Balcombe et al. [17] introduced the elastic deformation of the crack faces in the long crack propagation modeling using the finite volume/boundary approach. Akama and Mori [18] used the boundary element (BE) approach for the stress intensity factor determination of long cracks. The boundary condition of the half space that contains the surface breaking crack was determined using the analytical solutions of the simple radial distribution [19]. The friction between the crack faces and the fluid hydraulic pressure within the crack were included in the BE model.

Glodež et al [20, 21] included the crack propagation into the RCF modeling while considering only subsurface cracks. For the modeling of the short crack propagation, the approach of Navarro and Rios [22], and Sun et al. [23] was adopted. The virtual crack extension method [24] was employed in the finite element analysis for the determination of the stress intensity factor at the crack tip. Flašker et al [25, 26] studied the surface crack propagation including the EHL effects, assuming the hydraulic pressure within the crack is constant and the same as the EHL pressure at the crack mouth location. Kaneta and Murakami [27] modeled the three-dimensional crack propagation under lubricated Hertzian point contact condition, using the mixed mode fracture mechanics approach. Bogdanski et al. [28] and Bogdanski [29] also extended their two-dimensional model [14, 15] to the three-dimensional one.

In view of the above modeling studies, the mechanisms of the fatigue crack growth under the compressive stress condition is listed as [13]

- The cracks propagate in the mode II of shear, where the cyclic shear stresses dominate;
- The cracks open in mode I by the normal hydraulic pressure of the lubrication fluid exerting on the crack faces;
- The trapped fluid inside the cracks is pushed towards the crack tip, opening the cracks.

On the aspect of the experimental literature, the important observations for surface nucleated crack growth under combined rolling and sliding contact condition is summarized as

- The fatigue cracks propagate only if lubrication fluid is present [30-32]
- The cracks grow in the direction that is opposite to the direction of sliding [33, 34]

### 1.3 Thesis Objectives and Outlines

This study aims at the quantification of the impacts of the crack length, crack orientation, surface friction and loading condition on the surface nucleated micro-crack stress intensity factor behavior of a line contact problem. The finite element approach is used to construct the model. A sophisticated meshing scheme that consists of a three-stage meshing, i.e. a fine mesh zone in the vicinity of the micro-crack, a coarse mesh zone that

is far away from the micro-crack, and a transition zone in between, is developed to accurately and efficiently discretize contact body, allowing the fast and accurate solution.

The outline of this thesis is listed below:

- Chapter 2: The finite element model will be introduced in detail. The newly developed multi-stage meshing scheme and the finite element selection will be described. The detailed Hertzian and Sinusoidal surface loading condition will also be discussed.
- Chapter 3: The numerical simulation matrix will be constructed. The solution data set will be documented and discussed.
- Chapter 4: The research activity will be summarized. Conclusions and recommendations for future work will be provided.

# CHAPTER 2

# THEORY AND MODELING

This study focuses on the determination of the stress intensity factor (KIF), which dictates the crack propagation behavior, under assumed loading conditions, namely a Hertzian contact pressure distribution and a Sinusoidal contact pressure distribution. The former is for the description of the contact of smooth surfaces, and the latter is to imitate the contact of rough surfaces where the pressure fluctuates due to the surface irregularities [25, 26]. Additional surface tangential shear stress distributions are also implemented by assuming a constant friction coefficient across the entire contact zone. The associated applications of this study include the macro and micro pitting failures of bearing and gear contacts. For many automotive and aerospace applications, the size of the contact zone is usually small in comparison to the mechanical element (bearings and gears) itself, the interested body of a contact pair (for example: the pin of a rolling element bearing and the pinion of a mating gear pair, where the cracks nucleate first) thereby can be represented by a half space that is subject to the adopted load condition. In order to further simplify the problem and avoid the overwhelming computational efforts, the three-dimensional (3D) contact is reduced to a two-dimensional (2D) one by applying the plane strain condition,

which is a valid assumption in view of the large axial direction dimension of most bearings and gears in the fields.

For the modeling of the mechanical behavior of a crack tip, both the boundary element method (BEM) [18] and the finite element method (FEM) [24] have been the popular approaches. The boundary element method considers only the boundary of the contact body instead of the entire area [18], reducing the 2D problem further to a one-dimensional one. Therefore, the number of mesh elements can be substantially reduced, allowing a very fine mesh of the surface. However, the mathematical formulation and the integrals that involve singular kernels require complicated numerical treatments in BEM. As a result, there is limited number of BEM based software available to deal with the contact problem. The finite element method on the other hand is commonly employed when the contact of two bodies are considered or the material of the contact pair has nonlinear properties.

Numerous commercial FEM codes such as ANSYS, NASTRAN, RADIOSS, and ABAQUS are readily available for solving various contact problems. These finite element codes can numerically determine the contour plots for contact stresses and the Von Mises stresses in the contact body under both the cases of smooth and rough surface conditions. In FEM, the bodies in contact are discretized into small elements (axisymmetric, planar, brick, etc.), and the contacting surfaces are represented by the nodal sets of the contact and the target surfaces. By defining the appropriate material properties, the frictional coefficient magnitude, and the boundary and loading conditions, a suitable mesh is generated to solve for the stress and strain distributions according to the elasticity theory. For the handling of the non-linearity in any contact, the load is applied in a stepwise way.

This study uses the finite element method, namely the ANSYS software, to construct the model.

## 2.1 Finite Element Meshing Method

ANSYS is a powerful and effective engineering FEM tool, capable of handling complex structures and loading conditions. This study utilizes the ANSYS version 16.2 to create the FEM model that describes the mechanical behavior of the tip of a micro-scale crack in presence of a half space as shown in Figure 1. The half space here is modeled as a large semi-circle area whose radius $R$ is twenty times the half contact zone size $b$, i.e. $R = 20b$. As an example, the contact zone in Figure 1 is subject to a normal Hertzian pressure distribution $p$ and a tangential shear distribution $q$, both of which move along the surface to the left in a continuous way.

For the definition of the surface crack, the crack face length is $c$ and its orientation is represented by the angle between the crack face and the horizontal direction as $\Theta$. The distance between the surface crack mouth and the center of the contact zone is denoted as $a$. A global reference system $X$-$Y$ is made such that its origin is located at the lowest point of the semi-circle area as shown in Figure 1. The $X$ axis is along the horizontal direction and the $Y$ axis is in the vertical direction. A local coordinate system $x_c - y_c$ is established at the tip of the crack, with its $x_c$ axis pointing along the crack face with its crack face present in the negative axis, and its $y_c$ axis being normal to the crack face.

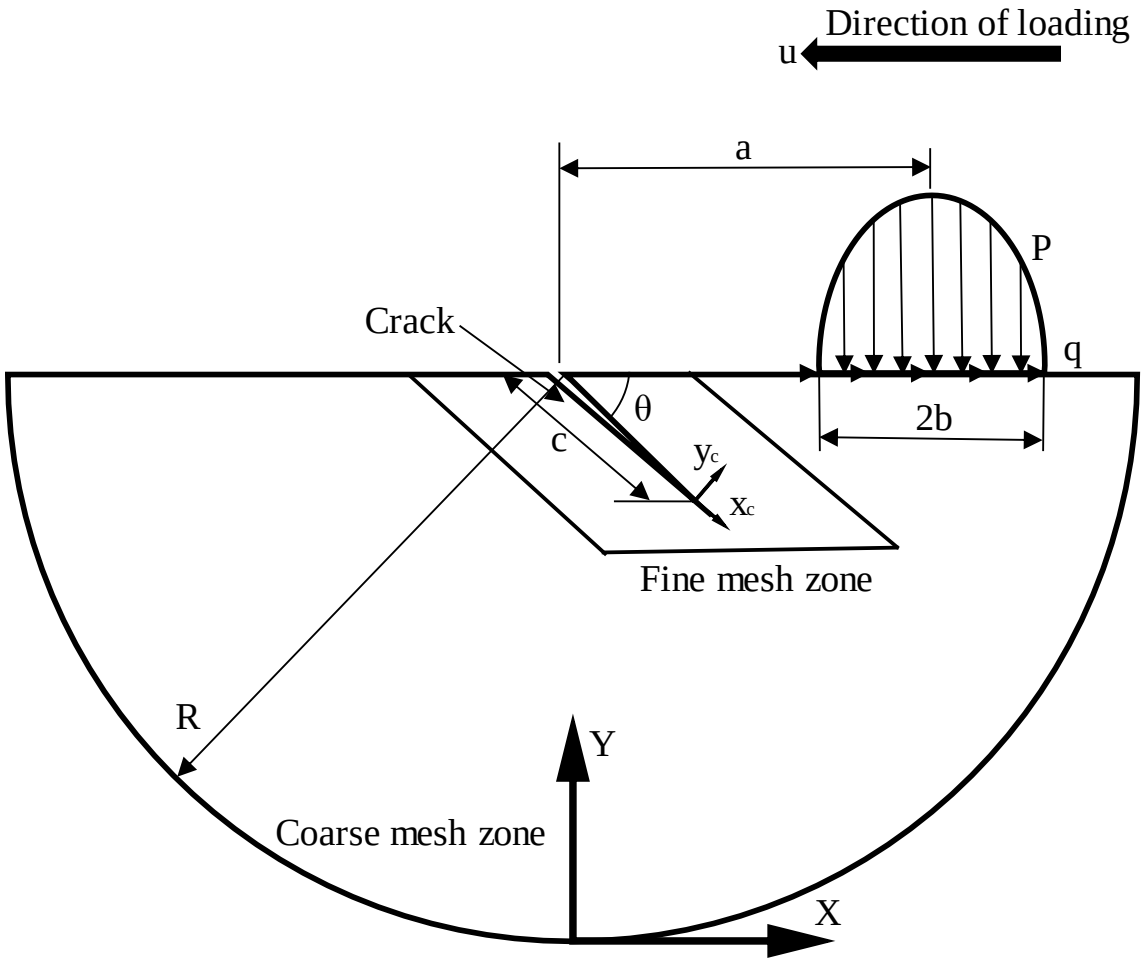


Figure 1: Configuration of the model.

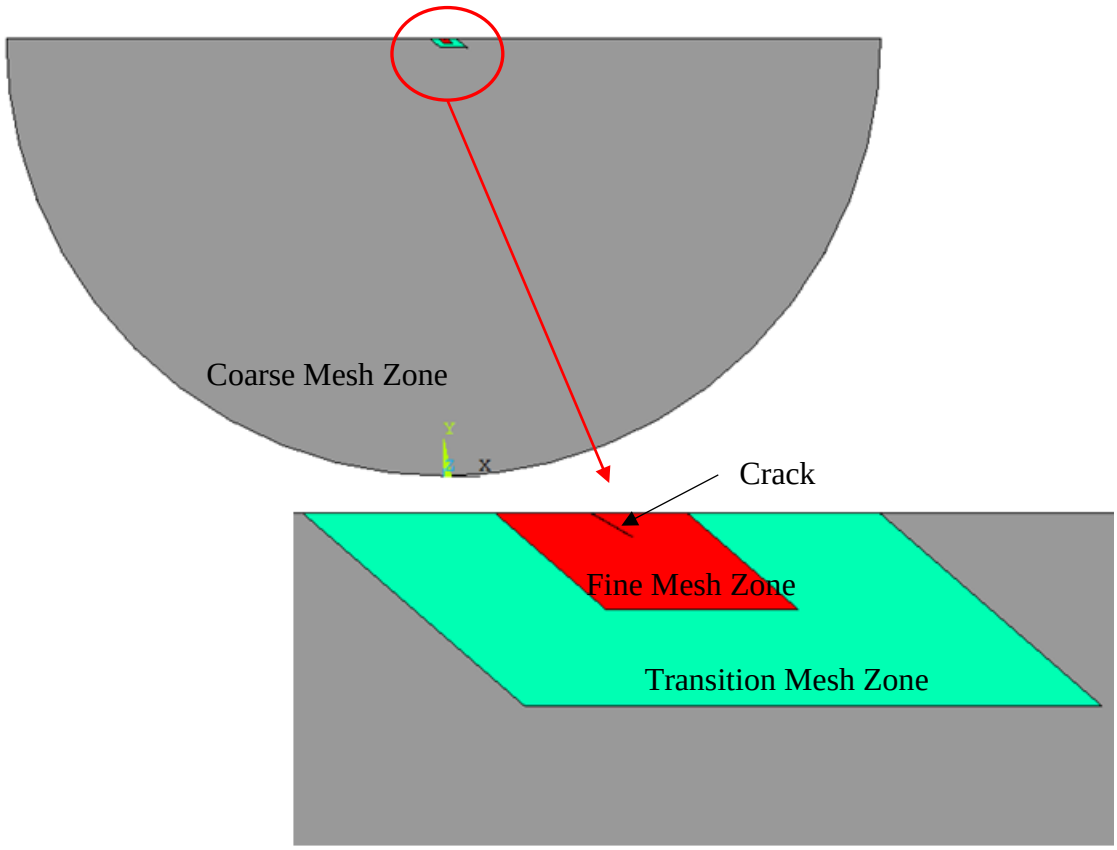


Figure 2: Area discretization at the Crack.

In order to accurately capture the displacements in the vicinity of the crack, which dictate the stress intensity factor, a parallelogram Fine Mesh Zone (FMZ) is implemented around the micro-crack as shown in Figure 2.

The left and right sides of the FMZ are set to be parallel to the crack face. The top side of the FMZ is along the surface and the bottom side of the FMZ is parallel to the surface. The dimension of each side of the FMZ is set to be proportional to the crack face length and equal to 2*c*. Because of the limited computer memory and computational power, a very fine mesh over the entire semi-circle area is not feasible. Therefore, a Coarse Mesh Zone (CMZ) is utilized to discretize the area that is far away from the crack in Figure 2.

Within this Transition Mesh Zone, the element size is set to increase continuously from the FMZ to the CMZ. Quadratic quadrilateral elements are used in the meshing for the better convergence results. Such a meshing scheme offers both the high accuracy in the vicinity of the crack tip and the affordable overall computational efforts.

The quality of the mesh created for a member is of great importance since it largely affects the analysis convergence and accuracy. The commonly used meshing scheme available in ANSYS is the default meshing method with smart sizing technique, which automatically produces a mesh using the element sizing quotient that is equal to six. The smart sizing technique can vary from one (finer mesh) to ten (coarse mesh). In the process, the user has control only on the sizing quotient and not on the number of the elements generated. The quality of the elements is neither guaranteed when a micro-size crack is present as shown in Figure 3. Due to the small size of the crack, the default meshing may simply ignore the presence of the micro-crack while meshing the member as illustrated in Figure 3 (a). Although this issue can be resolved by applying re-meshing around the crack,

the resultant elements associated with the upper crack face (master surface (contact) of the crack face contact) and elements associated with the lower crack face (slave surface (target) of the crack face contact) are not consistent with each other, i.e. not paired, as displayed in Figure 3 (b). As a result, the contact between the crack faces under loading cannot be appropriately modeled. Adjusting the sizing control does not rectify the quality of the resultant mesh.

To overcome this issue, the mesh improvement techniques available in ANSYS are chosen to generate considerably smaller elements in the local area of the crack region. Although the condition of the mesh can be improved to a certain extent, there is no control on the element sizing and nodes created. This method, therefore, does not suit for the considered problem due to the presence of a micro-scale crack.

An alternative meshing scheme is the mapped meshing method, which is carried out by manually discretizing the bounds of the meshing zones, including the fine mesh zone, the transition meshing zone and the coarse meshing zone as illustrated in Figure 2.

This discretization can be generated by defining either the number of divisions or the size of the division segment along the bounds as per the requirement of the mesh zone as shown in Figure 4. With the discretization details defined along the bounds, the mesh within each of the meshing zones can then be automatically created by ANSYS. This meshing method not only drastically improves the quality of the mesh by substantially reducing the number of the bad elements such as those obtuse and acute angle elements, but also allows the direct control of the number of the elements and the size of the elements. Both triangular and quadrilateral elements can be used with this method, depending upon the convergence criterion.

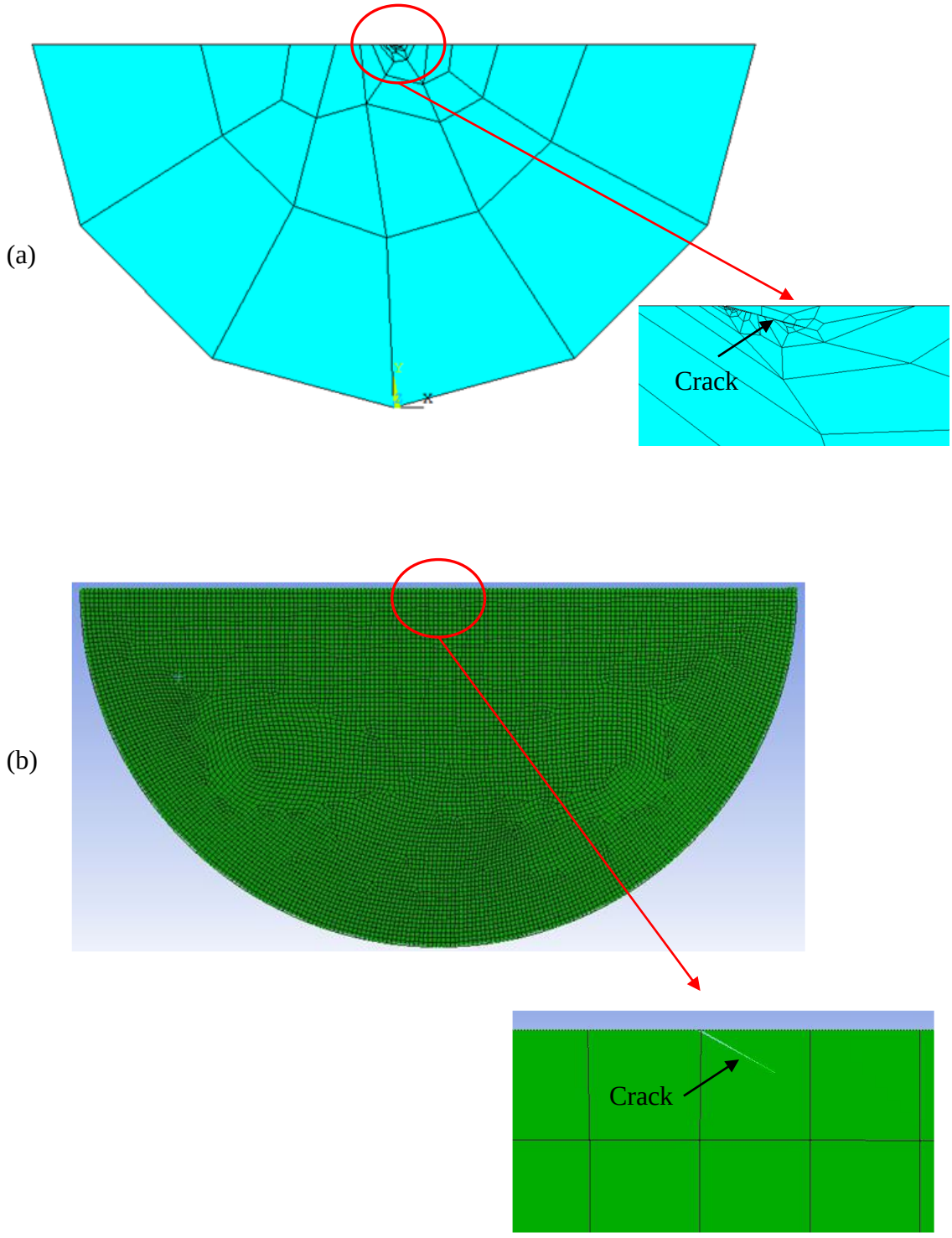


Figure 3: Default mesh in ANSYS (a) Re-meshing around Crack (b) Ignored mesh around Crack.

The number of the nodes generated are manually controlled by the number of elements. This is useful in creating the ANSYS Parametric Design Language (APDL) macro script and reading the results at the node level. Although the mapped meshing method provides superior convergence and accuracy performances over the default meshing method, the numerical solutions can only provide the stress and/or displacement contours around the crack. The detailed mechanical behavior at the crack tip that is required for the determination of the stress intensity factor cannot be easily obtained, owing to the missing of the sufficient number of dedicated elements connecting to the tip. Therefore, an additional meshing treatment is required focusing at the tip of the crack.

Since the element shape functions which transfer the boundary conditions and the loading conditions at the crack tip are essential for the simulation accuracy, this procedure is created so that the elements being generated adjacent to the singular elements at the crack tip can be quadrilateral or less faulty. The occurrence of the faulty elements greatly affect the convergence of the solution. Special attention is taken while creating the mesh near the crack region for better mesh quality minimizing the occurrence of faulty elements and to have equal number of elements on the crack opening lines. Crack face and crack tip are defined for finding out stress intensity factor at the crack tip. Mesh near the crack region and at the crack tip are shown in Figure 6.

A crack-tip-focused mesh has to be generated utilizing the singular elements surrounding the crack tip, such that the reference system can be shifted from the global one ($X$-$Y$) to the local one ($x_c - y_c$) at the crack tip to calibrate the localized results. The singular elements are created to store the singularity in the strain around the crack tip.

The displacements near the crack tip are on the order of $\sqrt{r}$, whereas the stress and strain are on the order of $1/\sqrt{r}$. In order to pick up the singularities in the strain, the elements must be quadratic with the mid-side nodes positioned at the quarter points as shown in Figure 5 [41]. According to Barsoum (1976,1977) [37, 38], by placing mid-side nodes at quarter point around the crack tip, the inverse square root singularity characteristic of Linear Elastic Fracture Mechanics (LEFM) can be obtained in iso-parametric elements. This study was further developed by Hussain, Lorensen and Pu (1978) [39] by adding 12-nodes to the quadrilateral iso-parametric elements. A transition element with the same property to obtain the singularity of order $1/\sqrt{r}$ is developed by Lynn and Ingraffea (1978) [40]. The ratio of the length of singular element to the length of the crack affects the accuracy of the stress intensity factor measured at the crack tip using singular elements. The singular behavior of the elements is not transferred to the neighboring non-singular elements around the crack tip when the ratio of the length of singular element to the length of the crack approaches a smaller value. A transition element with the same order of singularity at the crack tip are replaced with the non-singular elements around the singular elements as shown in Figure 5 [41].

The crack-tip focused mesh can be created by defining the KSCON command in ANSYS which allows to generate the focused mesh at the crack tip by using the option of skewed element for the produce of the singular elements. The following procedure is used in creating the focused mesh:

1. Create the mesh in the semi-circle (half space model) and create a concentrated mesh at the crack tip with Mesh-Size Control-Concentrated Key point option available in ANSYS.

2. Use *a*/8 as the radius of the first row defining the singular elements.
3. Use 1.5 as the radius ratio (2nd row/1st row) for defining the transition elements.
4. Use 8 or 16 for the number of elements around the circumference.
5. Use the Skewed 1/4-point option for the mid-side node position.
6. Use size control along the radial lines emanating from the crack and along the circumference of the semi-circle.

The resultant focused mesh with singular elements at the crack tip are generated through the above procedure as shown in Figure 6.

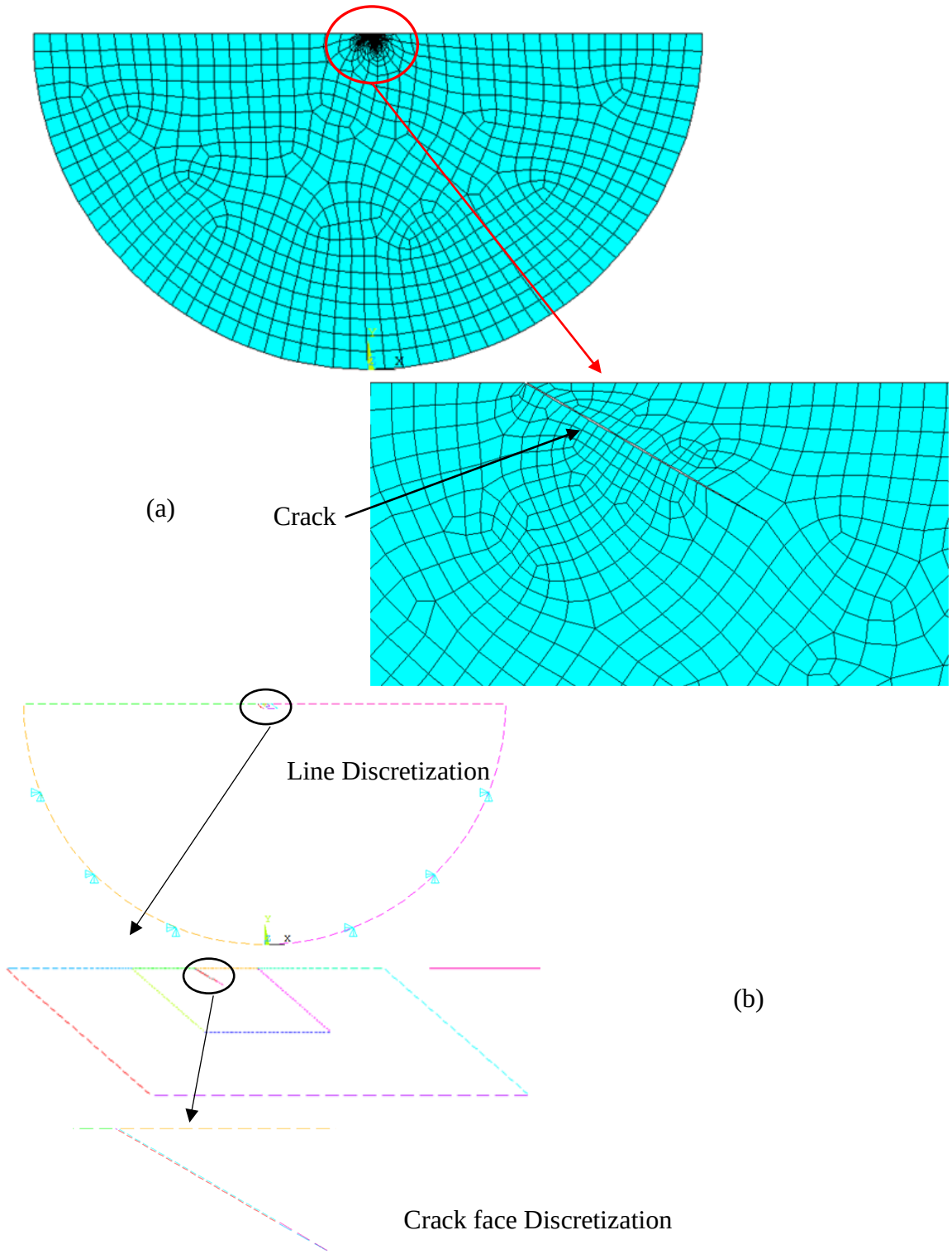


Figure 4(a): Mapped meshing in ANSYS (b): Line discretization of model.

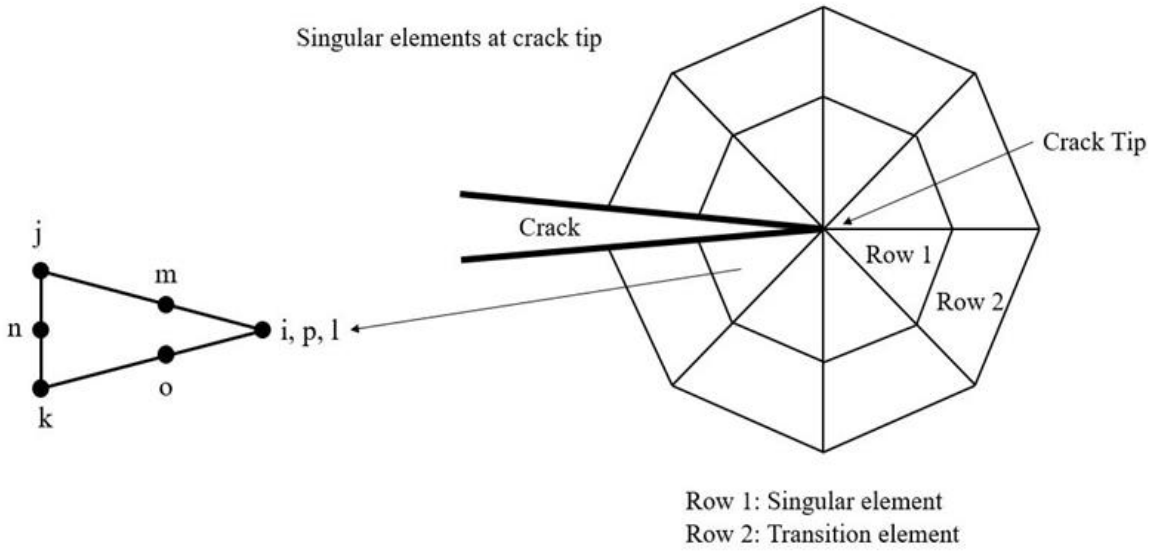


Figure 5: Definition of Singular elements.

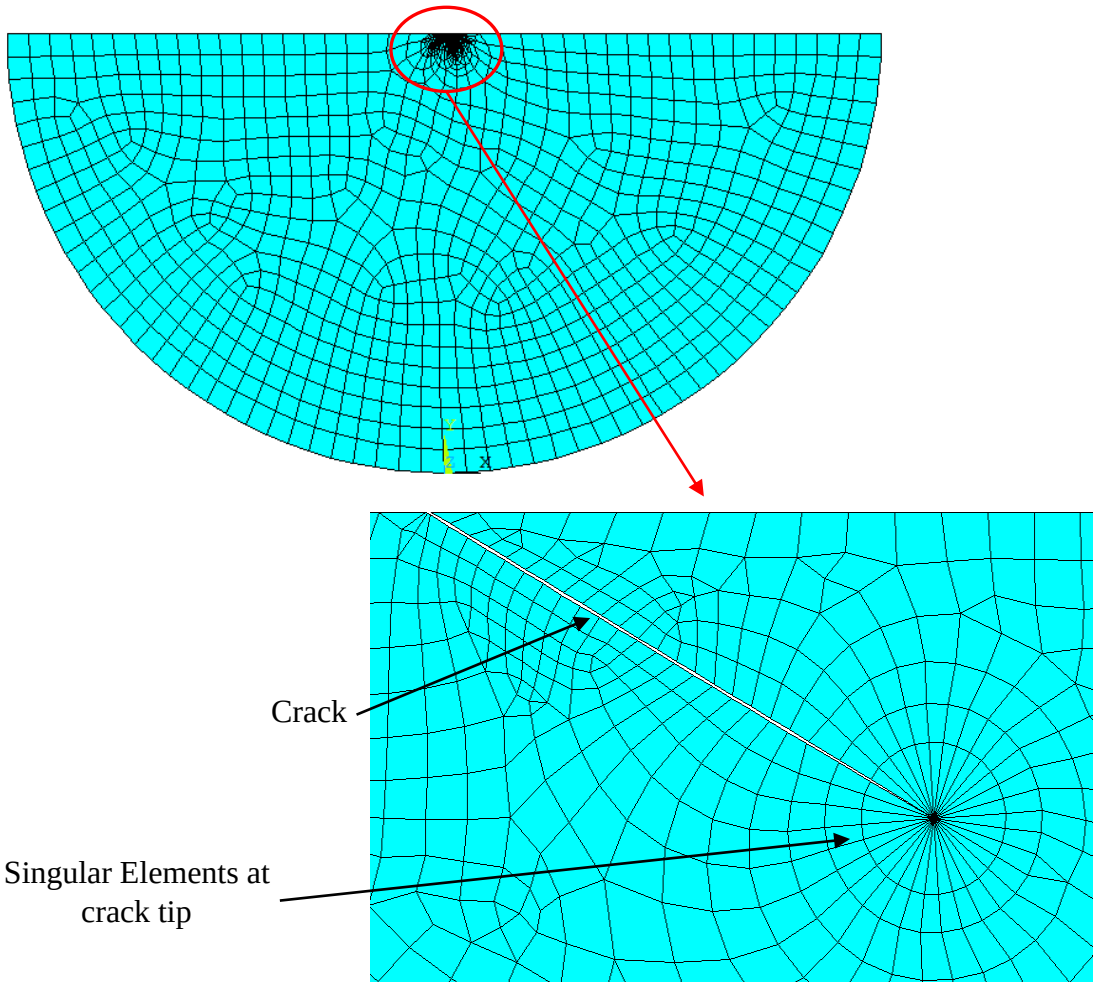


Figure 6: Focused mesh with Singular elements in ANSYS.

## 2.2 Finite Element Selection

ANSYS includes a variety of linear or higher-order basic element types with or without mid-side nodes. Linear elements or elements without mid-side nodes have extra shape functions at the corners and are used for performing structural analyses without degenerate forms or distorted elements in critical regions. For non-linear structural analyses, quadratic elements must be used. Quadratic elements have mid-side nodes which support degenerate element shapes and converge better in non-linear structural analyses as shown in Figure 7 [41]. While assigning elements to the model, care has to be taken in constraining the mid-side nodes. Mid-side nodes are to be connected with adjacent mid-sides only, keeping them in a straight line position as shown in Figure 8 (a) [41] and not to the corner nodes as shown in Figure 8 (b) [41].

To characterize crack tip singularity, quarter point elements with mid-side nodes are utilized. The element in ANSYS library which accommodates the requirements of this analysis is Plane-183. Plane-183 is a higher order 8 or 6 node 2-D element with mid-side nodes as shown in Figure 9 [41]. It has the capabilities of handling quadratic displacement behaviors and irregular meshes with acute or obtuse angled elements. Plane-183 is used as an axisymmetric element that has two degrees of freedom at each node (translations in nodal x and y direction) under the plane strain condition. Plane-183 also has the capabilities of modeling plasticity, stress stiffening, large deflection and large strains. This element can take up pressure loads as surface loads. The direction of the stresses acting on the element are parallel to the element coordinate system.

To define the crack tip opening and to determine the stress intensity factors at the crack tip, contact and target elements are defined on the crack faces to describe the contact and the sliding behavior between the two surfaces. When two surfaces move towards each other, the contact element is squeezed on to the target element, closing the initial gap. As there are several different contact and target elements in ANSYS, proper understanding of the contact analysis is required while creating a contact pair. Nodal sets for contact and target are created by selecting the nodes from the elements defining the contact and target surfaces. The contact nodes are those that will move into contact with the other surface, whereas the target nodes are those that are being contacted. Both the contact and the target surfaces have to be discretized in the form of node-node, node-surface or surface-surface elements depending on the complexity of the problem and the type of surfaces involved in contact as the smoothening of the surfaces by discretization provides a significant improvement in the convergence behavior. The number of nodes involved in the contact pair has to be limited in order to avoid the computational delays at arriving the solution.

The resulting contact pair should generally pass the patch test or the mesh discretization effects i.e., when a uniform pressure is applied on top of a surface, uniform stress state should be obtained irrespective of the mesh. It should also satisfy the Ladyshenskaja-Babuska-Brezzi (LBB) condition or the ability to handle over constraint criterion and also support contact with quadratic order elements. For this model TARGE-169 and CONTAC-175 are the element type chosen to define the contact pair. The CONTAC-175 is a surface element that can model both the contact and the sliding between the two surfaces or nodes under either the 2D or 3D condition. This element type uses mid-side nodes for supporting bonded and no separation type of contact boundary conditions.

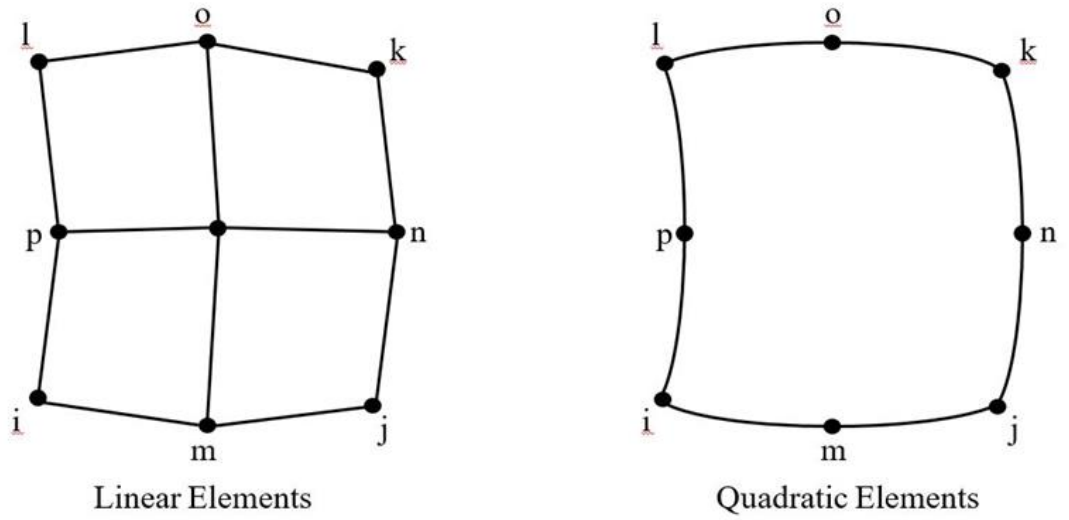


Figure 7: Linear and Quadratic Elements.

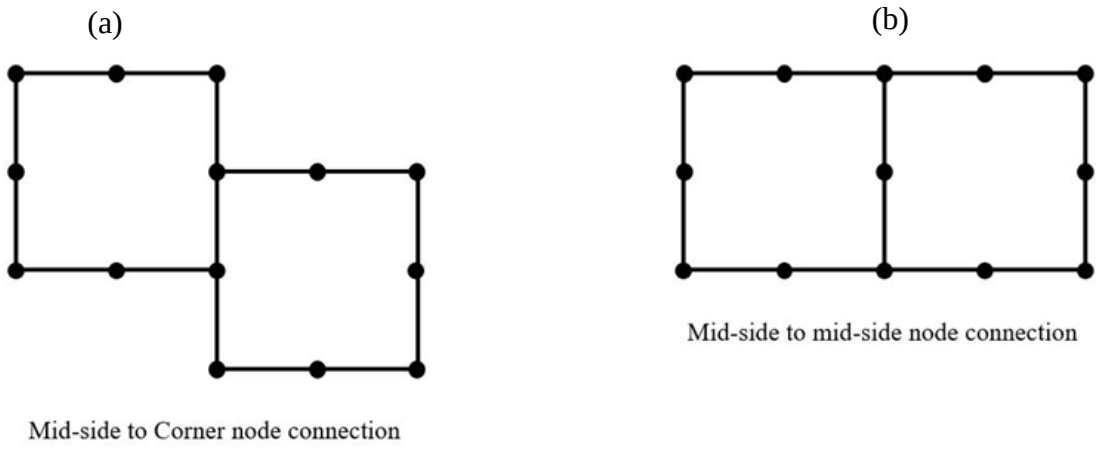


Figure 8 (a): Mid-side to corner node connection (b) Corner node connections.

This element type supports both the rigid and the flexible deformable surfaces which is suitable in case of a dissimilar mesh pattern on both sides of contacting surface. The contact between the elements is possible only when the outward normal direction of the target surface points to the contact surface as shown in Figure 10 [41]. Due to this property, a localized coordinate system $x_c - y_c$ is created at the crack tip for the contact stresses to be transmitted across the contacting surfaces. This element can handle pure Lagrange, augmented Lagrange or pure penalty algorithms which allow tiny penetrations.

A user defined contact normal direction can be generated. TARGE-169 is a 2D target surface element that is paired with the contact element to form a contact pair. This element type also supports both the rigid and the deformable surfaces. The target surface comprises a set of nodes, each of which must be associated with its unique contact node along the contact surface as shown in Figure 11 [41]. The boundary conditions can be imposed on these target elements and nodes depending on the type of problem being considered. It is noted, however, the constraining equations cannot be used on these type of elements.

A contact pair is created between the crack faces to simulate the problem by implementing the target and surface elements. When the load applied passes over the crack region, the crack faces come in to contact, impacting the stress state at the crack tip. If the contact pair is not generated properly, the crack faces can penetrate each other when the load is large or the crack faces do not touch each other when the load is too small. The model can become unstable and can produce wrong results in either of the cases. It is difficult to generate a good contact pair since the contact stiffness fluctuates greatly along the crack face due to the coexistence of the local no contact nodes (zero stiffness) and the

local contact nodes (large stiffness). This contact stiffness fluctuation is depending on the dimension and the orientation of the crack faces, as well as the loading condition.

To ensure the quality of the contact-target pair generated, the following procedure is implemented:

1. Select a nodal set to represent the contacting surface which is the deformable surface.
2. Select a nodal set to represent the target surface which is a rigid surface.
3. Establish contact settings by selecting the coefficient of friction between the surfaces.
4. Choose a behavior of contact surfaces depending on the boundary conditions.

Since the contact and target surface are assumed to be rigid-flexible in nature, a node-surface type of contact is established. The point-edge contact model is defined by the node-surface contact which enables contact around corners also.

Default behavior of contact surfaces settings were chosen for this analysis to simulate the problem. The default settings include using Augmented Lagrange algorithm and standard contact behavior of contact surface with the contact normal, normal to the target surface. Augmented Lagrange method is less expensive and more robust and allows element superposition if required. The method augments the contact force or pressure calculations by$F_{normal} = k_{normal} * x_{penetration}$, where $F_{normal}$ is the finite contact force and $k_{normal}$ is the contact stiffness and $x_{penetration}$ is the distance of penetration of the contacting surfaces. Augmented method is suited for ant type of contact behavior and uses either iterative or direct solvers for both symmetric and asymmetric contacts. A normal

contact stiffness equal to the product of contact length and elastic modulus of the underlying elements is chosen.

A penetration tolerance equal to the product of contact length and 5e-3 is given. A frictional coefficient of 0.1 is assumed for this model. The standard contact behavior of contact surface is best suited when the contact and target surfaces are initially in open contact condition, which is the initial condition of this model. The standard contact behavior also provides resistance to reduce the risk of rigid body motion. The rigid body motion also depends on the damping coefficients selected for the analysis which should not be too large or too small. But the ideal values depend on the specific problem, the time of the load step and the number of the sub steps.

The number of load steps and the time of the load step is to be decided by the application of the load. For this half space model, since a Hertzian and Sinusoidal pressure load is being applied, the load should be applied in the form of a stepped or a ramped loading. If a load is stepped, the full value of the load is applied at the first sub step and stays constant for the rest if the load step as shown in Figure 12(a) [41] and if the load is ramped, the load value increases gradually at each sub step with the full value occurring at the end of the load step as shown in Figure 12(b) [41]. From the Figure 12 [41], ramped loading is the appropriate loading for the transient analysis of the half space model. The number of load steps for the analysis and the number of sub steps with in each load step are to be decided by the user depending on the computational capacity of the system configuration without compromising the solution.

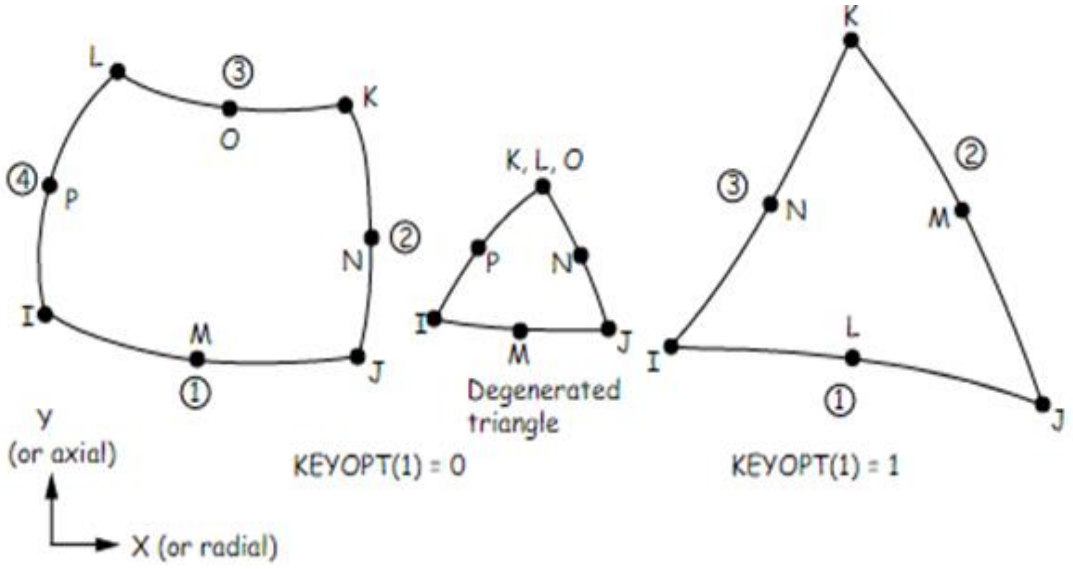


Figure 9: Plane 183 elements with mid-side nodes.

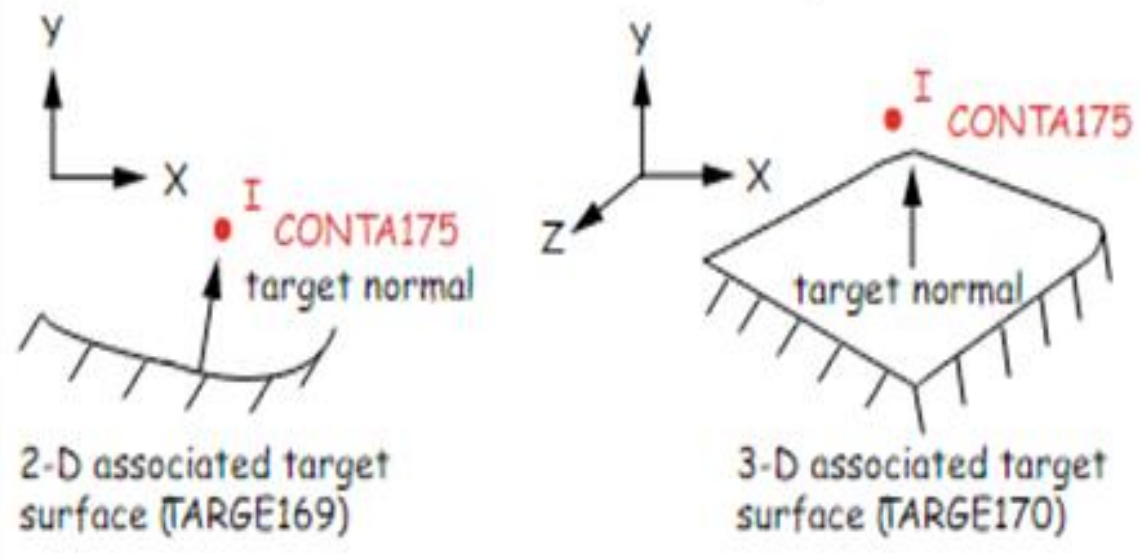


Figure 10: Representation of contact element.

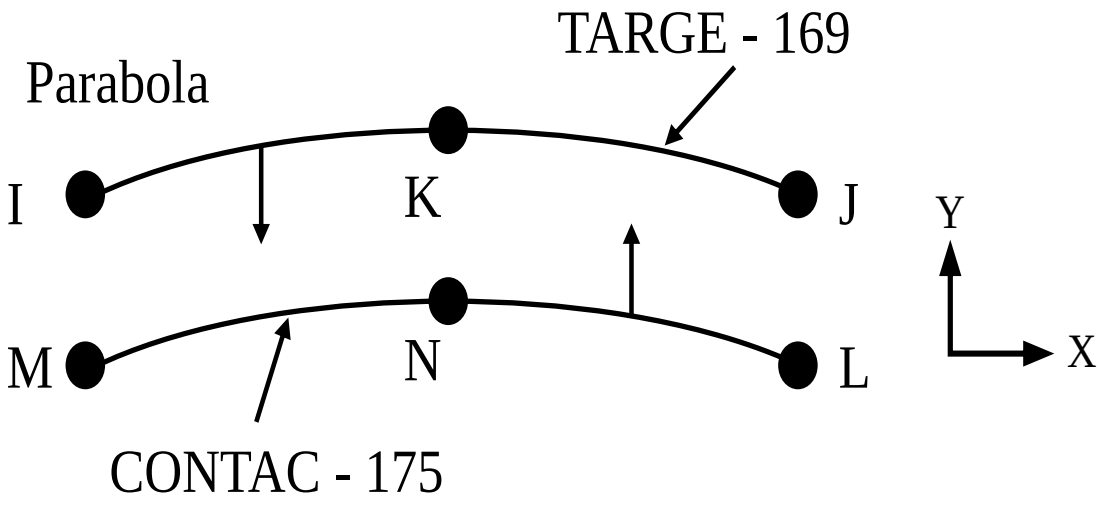


Figure 11: Representation of Target element.

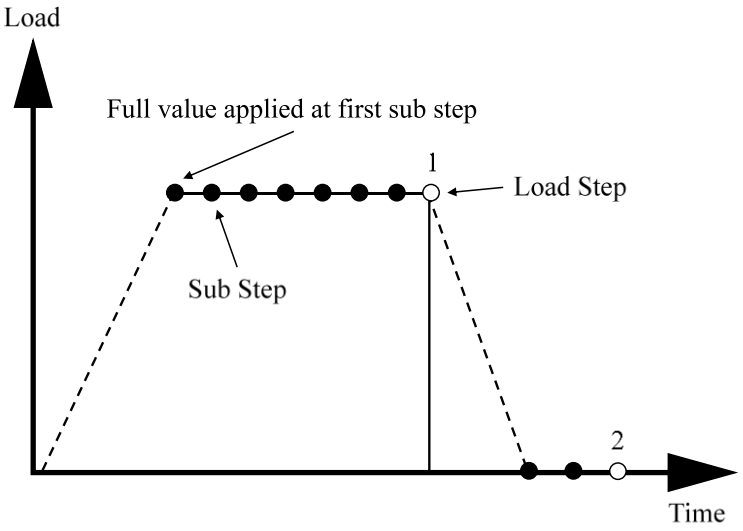


(a)

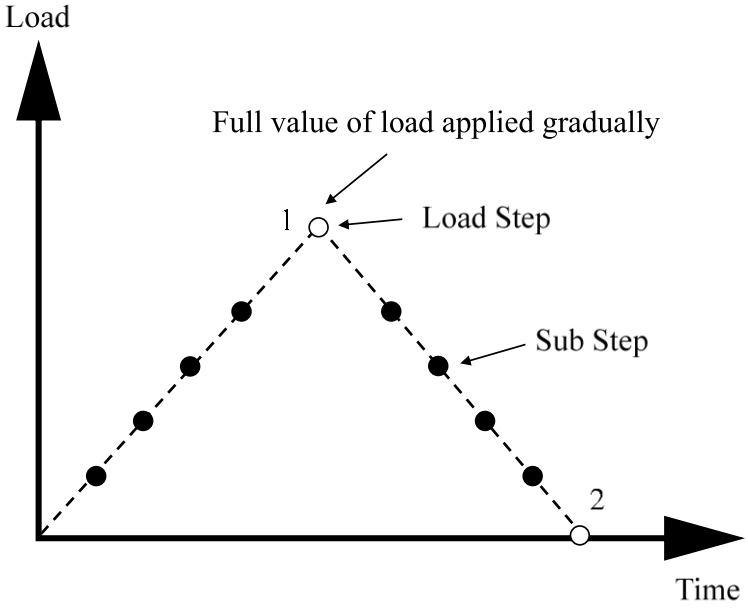


(b)

Figure 12 (a): Stepped loading (b): Ramped Loading.

## 2.3 Loading Conditions

In automotive and aerospace applications, both the bearing and gear contacts commonly operate under the elasto-hydrodynamic lubrication (EHL) condition, where the entrained lubricant film protects the solid surfaces from direct metal-to-metal contacts. Under the perfectly smooth surface condition, the existence of the lubrication film does not largely change the contact pressure. The resultant normal pressure distribution actually is in relatively good agreement with the Hertzian pressure distribution, especially in the center of the contact where the pressure is high. Since the contact simulation involving the elasto-hydrodynamic lubrication is computationally demanding, this study neglects the EHL and utilize either the Hertzian contact pressure distribution for smooth surface contacts or Sinusoidal pressure distributions for rough surface contacts.

The elastic contact between smooth curved surfaces can be described by the Hertzian theory. Figure 13 [41] shows an example contact between two semi-spheres under the normal load *W*. Body 1 has the radius $r_1$, the elastic modulus $E_1$ and Poisson's ratio $\upsilon_1$, and body 2 has the radius $r_2$, the elastic modulus $E_2$ and Poisson's ratio $\upsilon_2$. The initial separation between the two surfaces before *W* is applied, which is due to the curvature of the mating surfaces, is location dependent as

$$g_0 = \frac{x^2 + y^2}{2r'} \tag{2.1}$$

where $r'$ is the equivalent curvature and is defined as

$$r' = \frac{r_1 r_2}{r_1 + r_2} \tag{2.2}$$

After the compressive normal load *W* is applied, the contact pressure, *p*, is produced within a circular Hertzian zone, whose radius is *b*, between the mating surfaces. This normal pressure is also a function of the location, i.e. $p = p(x, y)$. With this loading distribution, the normal surface deflection of body 1, $u_1$, and the normal surface deflection of body 2, $u_2$, are generated. To compensate these deformations and maintain the in-contact condition of the two bodies, the rigid body approach, $\alpha$, takes place as illustrated in Figure 14.

As a result, the separation between the two surfaces after the load is implemented can be described as

$$g(x, y) = g_0(x, y) - \alpha + u_1(x, y) + u_2(x, y) \tag{2.3}$$

To solve such a contact problem, the equilibrium condition

$$W = \int_{x^2 + y^2 \le b^2} p(x, y) dx dy \tag{2.4}$$

and the boundary conditions within the contact zone of $x^2 + y^2 \le b^2$

$$g(x, y) = 0 \tag{2.5a}$$

$$p(x, y) \ge 0 \tag{2.5b}$$

and outside the contact zone of $x^2 + y^2 > b^2$

$$g(x, y) > 0 \tag{2.6a}$$

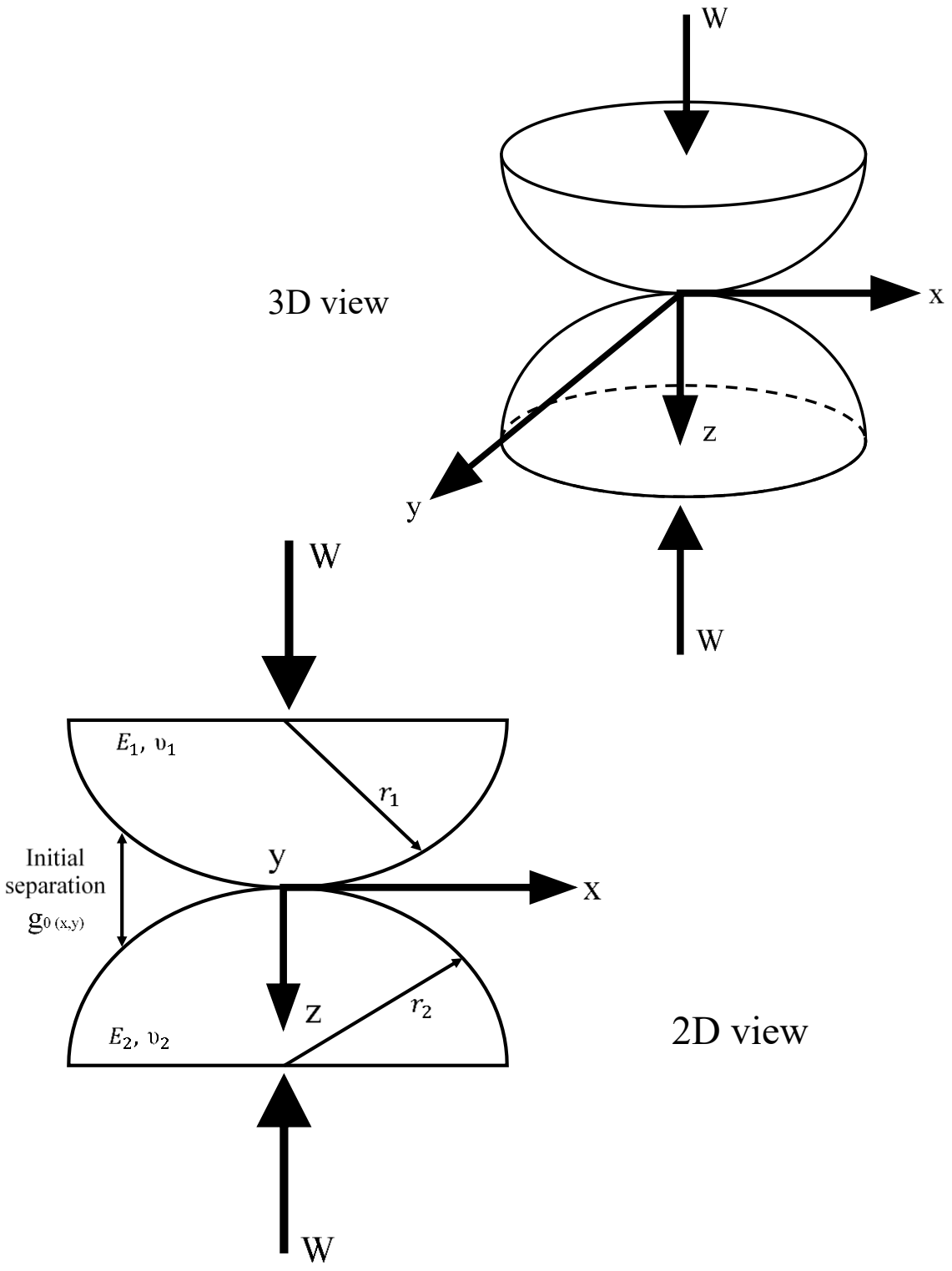


Figure 13: Contact between two semi-spheres under the normal load.

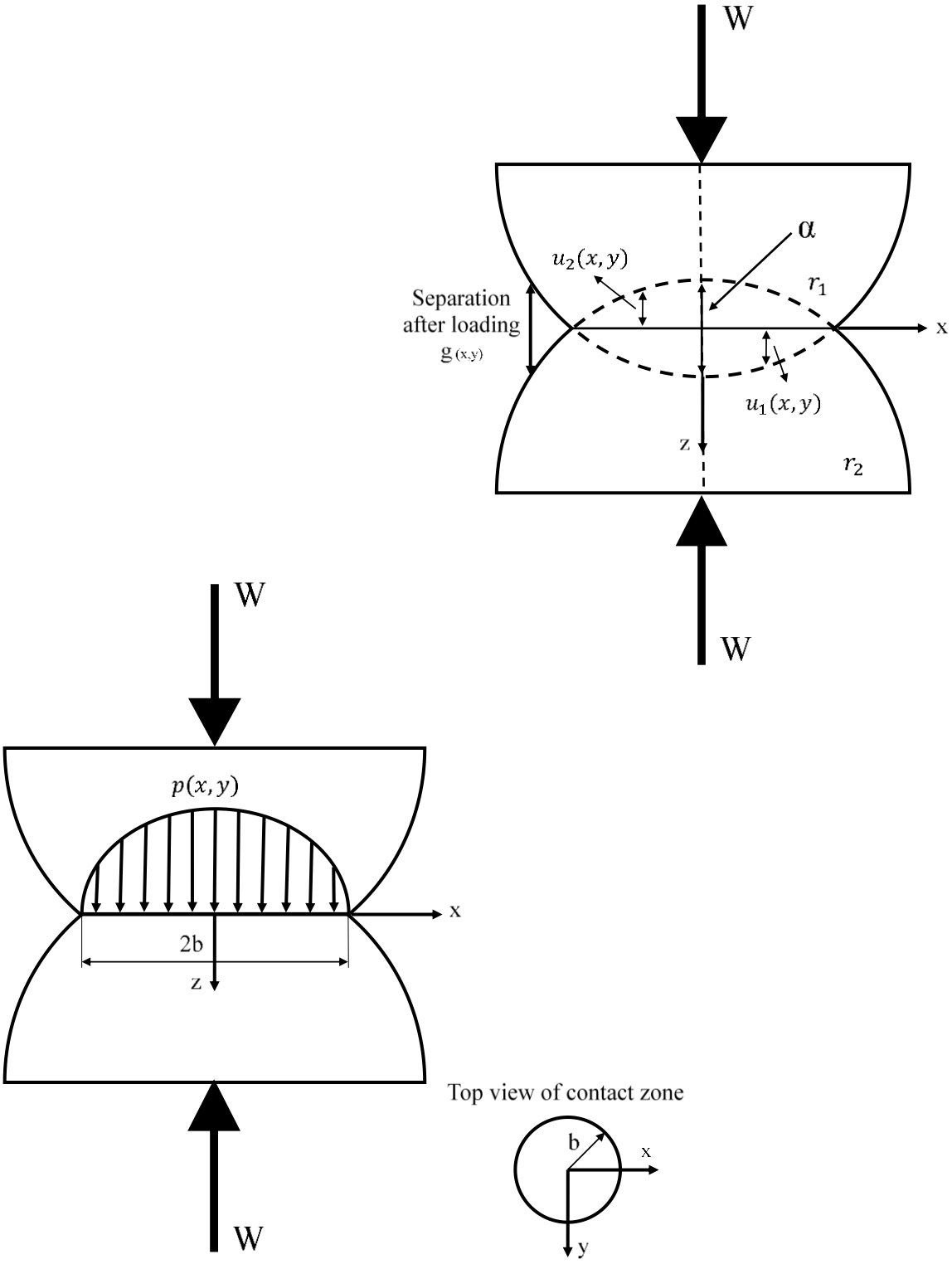


Figure 14: Hertzian contact zone under normal loading.

$$p(x,y)=0 \tag{2.6b}$$

are required to be solved together. The normal deflections in Equation (2.3) can be determined according to the Boussinesq fundamental solutions that have the expressions of [contact mechanice]

$$u_1(x,y)=\int_{x'^2+y'^2\le b^2}\frac{p(x',y')dx'dy'}{2\pi G_1}\frac{1-\upsilon_1}{2r} \tag{2.7a}$$

$$u_2(x,y)=\int_{x'^2+y'^2\le b^2}\frac{p(x',y')dx'dy'}{2\pi G_2}\frac{1-\upsilon_2}{2r} \tag{2.7b}$$

where $G_1$ and $G_2$ represent the shear modulus of body 1 and body 2, respectively, and $2r=\sqrt{(x-x')^2+(y-y')^2}$. By numerically solving the above equation sets, the contact pressure distribution and the contact zone dimension can be determined. For the very simple circular point contact, such as the sphere-on-sphere contact, the closed-form solutions can be obtained as

$$p(x,y)=p_{\max}\sqrt{1-\frac{x^2}{b^2}-\frac{y^2}{b^2}} \tag{2.8}$$

where the maximum Hertzian pressure

$$p_{\max}=\frac{3W}{2\pi b^2} \tag{2.9}$$

and the Hertzian half width

$$b=\sqrt[3]{\frac{3Wr'}{2E'}} \tag{2.10}$$

with the equivalent elastic modulus defined as

$$E' = \frac{2}{\frac{1-\upsilon_1^2}{E_1} + \frac{1-\upsilon_2^2}{E_2}} \tag{2.11}$$

When same material property is assumed for the contacting bodies, which reduces Eq. (2.11) to

$$E' = \frac{E}{\left(1-\upsilon^2\right)} \tag{2.12}$$

For a 2D contact problem such as the contact between two cylinders whose length is $L$, the Hertzian pressure can be obtained in a similar way as

$$p(x) = p_{\max}\sqrt{1-\frac{x^2}{b^2}} \tag{2.13}$$

where the maximum Hertzian pressure

$$p_{\max} = \frac{2W}{\pi bL} \tag{2.14}$$

and the Hertzian half width

$$b = \sqrt{\frac{8Wr'}{2E'L}} \tag{2.15}$$

When a more general contact case is encountered, a contact between two cylinders with the circular crown applied along the axial direction is considered where the resulting Hertzian contact zone is in the form of an ellipse.

The maximum Hertzian pressure $P_{\max}$ is determined as

$$P_{\max} = 1.5\frac{W}{\pi ab} \tag{2.16}$$

Where $W$ is the normal contact force, and $a$ and $b$ are the major and minor axes of the ellipse as shown in Figure 14 and determined as

$$a = C_a \sqrt[\frac{1}{3}]{\frac{1.5W}{2rE'}} \tag{2.17a}$$

$$b = C_b \sqrt[\frac{1}{3}]{\frac{1.5W}{2rE'}} \tag{2.17b}$$

Where $E'$ is the reduced elastic modulus of the contact body 1, whose elastic modulus is $E_1$ and Poisson's ratio is $\upsilon_1$, and the contact body 2, whose elastic modulus is $E_2$ and Poisson's ratio is $\upsilon_2$, as in (2.11).

In Eq. (2.17), $r$ is a geometry related parameter and is defined as

$$r = \frac{1}{r_1} + \frac{1}{r_1'} + \frac{1}{r_2} + \frac{1}{r_2'} \tag{2.18}$$

Where $r_1'$ and $r_2'$ are the radii of the circular crown implemented for the cylinders. The coefficients $C_a$ and $C_b$ in Eq. (2.17) are determined according to the Table 1 with $\beta$ defined as

$$\beta = \cos^{-1}\left(\frac{r'}{r}\right) \tag{2.19}$$

Where

$$r' = \sqrt{\left(\frac{1}{r_1} - \frac{1}{r_1'}\right)^2 + \left(\frac{1}{r_2} - \frac{1}{r_2'}\right)^2 + 2\left(\frac{1}{r_1} - \frac{1}{r_1'}\right)\left(\frac{1}{r_2} - \frac{1}{r_2'}\right)\cos(2\theta)} \qquad (2.30)$$

The angle $\theta$ in Eq. (2.30) is the angle between the plane containing $r_1$ and $r_2$, and the plane containing $r_1'$ and $r_2'$. In this study, the 2D Hertzian pressure distribution of Equation (2.13) is implemented with $p_{\max} = 1$ MPa and $b = 0.1$ mm for the smooth surface condition. The additional shear stress distribution is defined as

$$\tau = \mu p(x) \qquad (2.16)$$

where the coefficient of friction $\mu$ in this case is 0.1.

For the case of smooth surfaces, two loading cases are considered for this study: Hertzian pressure loading with traction, Hertzian pressure loading without traction. Figure 15 (a) shows the combined loading of Hertzian pressure distribution with surface traction acting along the surface of the half space model. Figure 15 (b) shows the Hertzian pressure distribution without the application of surface traction.

For a 2D contact problem such as the contact between two cylinders whose length is *L*, the Sinusoidal pressure can be obtained in a similar way as

$$p(x) = p_{\max} \operatorname{Sin}\left(\frac{\pi x}{b}\right) \qquad (2.17)$$

where the maximum Hertzian pressure

$$p_{\max} = \frac{2W}{\pi bL} \tag{2.18}$$

| β | $C_a$ | $C_b$ |
|---|---|---|
| 0 | ∞ | 0 |
| 0.5 | 61.4 | 0.1018 |
| 1 | 36.8 | 0.1314 |
| 1.5 | 27.48 | 0.1522 |
| 2 | 22.26 | 0.1691 |
| 3 | 16.5 | 0.1964 |
| 4 | 13.31 | 0.2188 |
| 6 | 9.79 | 0.2552 |
| 8 | 7.86 | 0.285 |
| 10 | 6.604 | 0.3112 |
| 20 | 3.778 | 0.408 |
| 30 | 2.731 | 0.493 |
| 35 | 2.397 | 0.53 |
| 40 | 2.136 | 0.567 |
| 45 | 1.926 | 0.604 |
| 50 | 1.754 | 0.641 |
| 55 | 1.611 | 0.678 |
| 60 | 1.486 | 0.717 |
| 65 | 1.378 | 0.759 |
| 70 | 1.284 | 0.802 |
| 75 | 1.202 | 0.846 |
| 80 | 1.128 | 0.893 |
| 85 | 1.061 | 0.944 |
| 90 | 1 | 1 |

Table 1: Coefficients for Hertzian contact width.

and the Hertzian half width

$$b = \sqrt{\frac{8Wr'}{2E'L}} \tag{2.19}$$

For the case of rough surface condition, only one case of loading condition is considered for this study: Sinusoidal loading without traction. Sinusoidal loading with traction is not considered for comparison due to computational consistencies and convergence issues. Figure 16 shows the Sinusoidal loading without surface traction.

The transient loading in ANSYS can be simulated by defining a simple load function with the help of Equation (2.13) and (2.16) for Hertzian pressure distribution with surface traction and Eq. (2.13) for Hertzian pressure distribution without surface traction. The Sinusoidal pressure distribution is defined by the Equation (2.17).

The load can be applied in two ways for pressure distribution as discussed below:

a) Create a load function according to the selected pressure distribution and apply the load in ramped form with respect to the length of the crack.
b) Create a load step in the form of transient load or ramped load with subsequent sub-steps by creating a load file with respect to the length of the crack.

In some transient load cases, combination of both the methods is also observed. For this study, a load function is created and applied as maximum pressure as shown in Figure 15 and Figure 16.

(a)

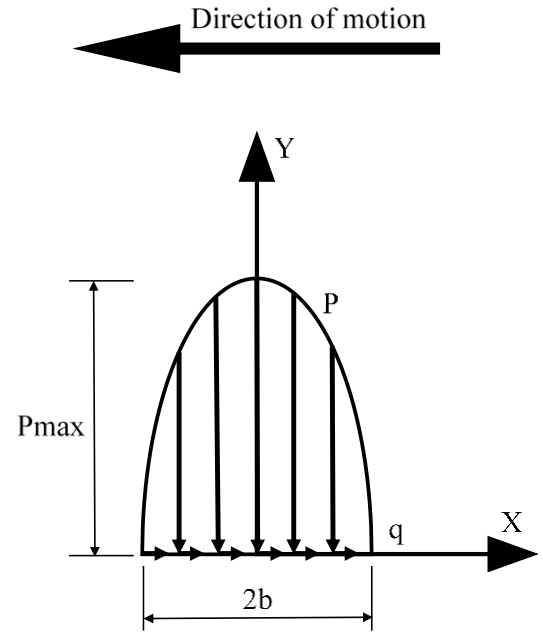


Hertzian Pressure Load with Surface Traction

(b)

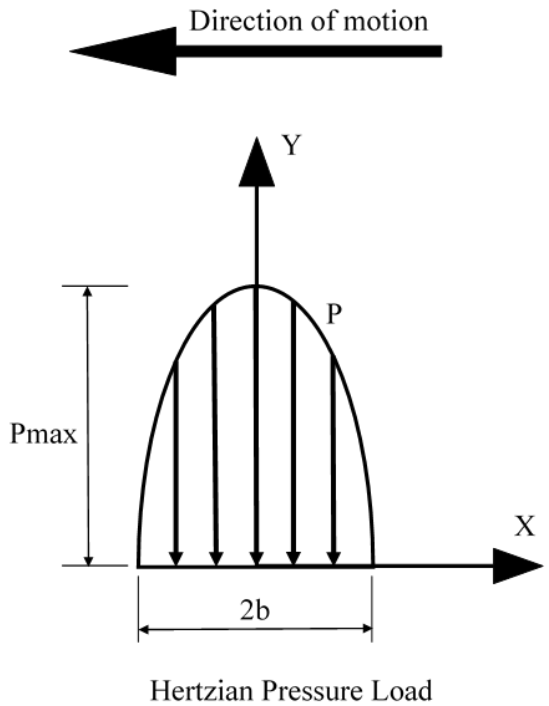


Hertzian Pressure Load

Figure 15: (a) Hertzian pressure loading with traction (b) Hertzian pressure loading without traction.

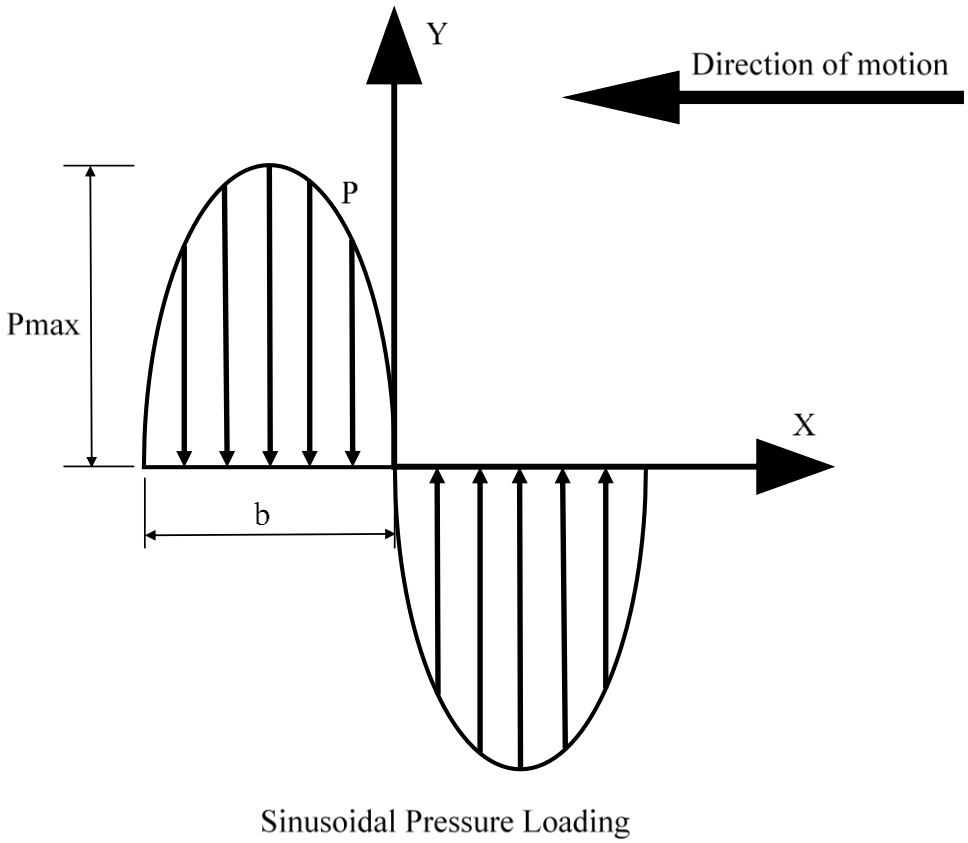


Figure 16: Sinusoidal pressure distribution without surface traction.

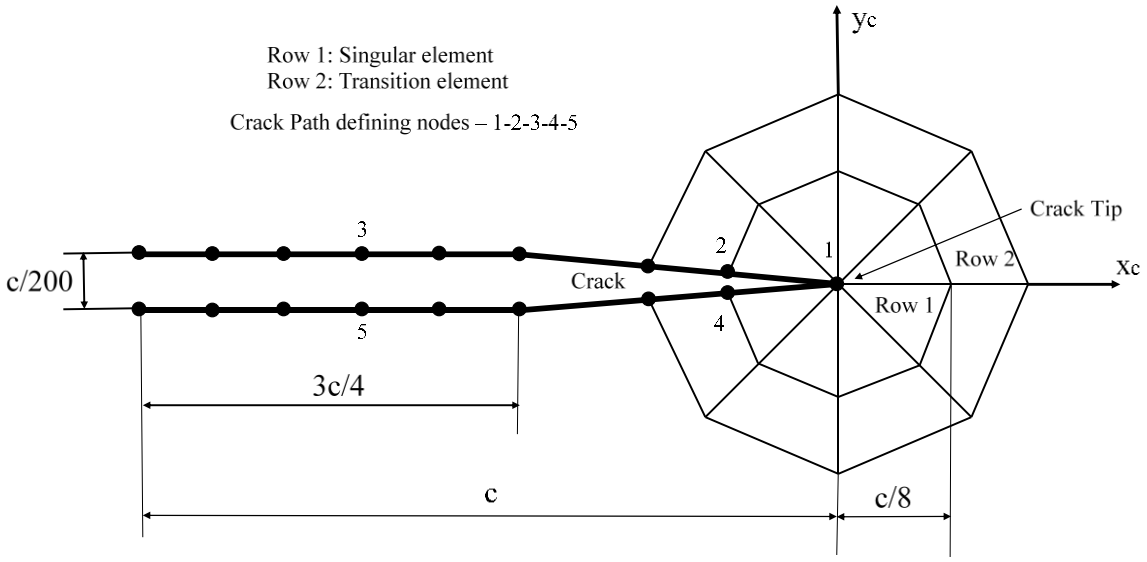


Figure 17: Dimensions of the Crack opening.

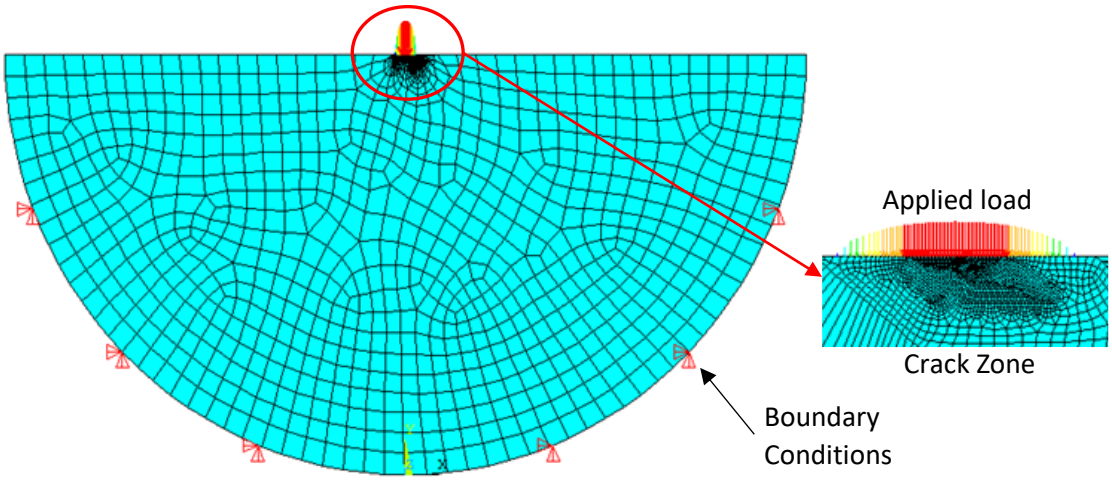


Figure 18: FEM model with boundary and loading conditions.

Elemental material properties are assigned and the analysis is to be carried out in plain strain condition since the model is in 2D condition. Material assumed is Steel with Young's modulus E = 2.1E5 N/mm$^2$ and Poisson's ratio $\mu = 0.3$.

To define the micro scale crack faces in ANSYS, a small opening of the crack is to be generated with a crack tip to accommodate singular elements. The crack boundary is created according to the Figure 17 [42]. The nodes generated on the crack faces are used in defining the crack path for ANSYS to define the local coordinate system $x_c - y_c$ at the crack tip. The nodes are also used in identifying the contact and target surfaces in order to define a contact pair. The dimensions of the micro crack opening depend on the length of the crack *c* as shown in Figure 17 [42].

For the establishment of the 2D FEM model displayed in Figure 1, the ANSYS Parametric Design Language (APDL) macro script is used to perform the coding, allowing the iterative simulations to calculate the stress intensity factor. After applying the fixed boundary condition at the bottom, an example normal Hertzian pressure distribution at the top surface, the fine mesh in the vicinity of the crack, and the coarse mesh away from the crack, Figure 18 illustrates the model developed. It is seen the mesh density in the fine mesh zone is significantly larger than that in the coarse mesh zone.

# CHAPTER 3

## RESULTS AND DISCUSSION

The transient behavior of the stress intensity factors (SIF) is investigated under the different loading distributions (Hertzian and Sinusoidal), considering different crack lengths and crack orientations. A simulation matrix is constructed in Table 2, where two crack orientation angles, $15^{\circ}$ and $30^{\circ}$, and two crack length values, 10 μm and 20 μm, are employed. For both the Hertzian pressure and the Sinusoidal pressure distributions, the maximum pressure is set at 1 MPa. To exam the impact of the surface friction (excluding the crack faces) on the SIF, two friction coefficient values of 0.1 and 0.3 are used. The friction coefficient between the crack faces is assumed to be fixed at 0.1. The response of the simulations are the Mode I and Mode II SIFs as the pressure distribution moves along the surface.

In the simulation, the moving direction of the load is set to be along the negative X-axis direction as shown in Figure 19, such that the pressure distribution initially sits on the right side of the crack mouth, then passes through the crack mouth location, and lastly stops at the left side of the crack mouth. In the process, the crack mouth that is initially open first closes as the compressive loading approaches and then reopen as the pressure distribution leaves. During the contact between the crack faces, the relative shearing

between the contact surface and the target surface occurs when the crack face tangential traction exceeds the static friction limit. The adopted contact elements prevent the surfaces from penetrating each other and avoid warping of the surfaces. Two loading analyses representing the smooth (Hertzian pressure distribution) and the rough (Sinusoidal pressure distribution) surface conditions are considered in this study. The surface tangential friction and normal pressure distributions determine the variation in the crack shearing action or $K_{II}$ (mode II of SIF). Previous studies showed that the shearing action is the dominant one when the coefficient of friction at the crack face is relatively low; while the tensile action or $K_I$ (mode I of SIF) is dominant under the circumstances of trapped fluid inside the closed crack, which expands at the crack tip, resulting in the mode I crack opening. The crack angles considered are acute (15° and 30°) to the load direction which causes the crack faces to close and open when the load passes over the crack mouth as shown in Figure 19 (a), (b) and (c). This crack orientation set-up doesn't facilitate the flowing of the lubricant into the open crack. The effects of fluid penetration induced mode I crack opening mechanism is thus excluded in this study.

| Parameter | Value |
|---|---|
| Crack angle (°) | 15, 30 |
| Crack length (μm) | 10, 20 |
| Hertzian pressure load (MPa) | 1 |
| Sinusoidal pressure load (MPa) | 1 |
| Friction between crack faces | 0.1 |
| Friction of the rolling contact | 0.1, 0.3 |
| Elastic Modulus (GPa) | 200 |
| Contact width of the pressure (μm) | 20 |

Table 2: Parameters in analysis.

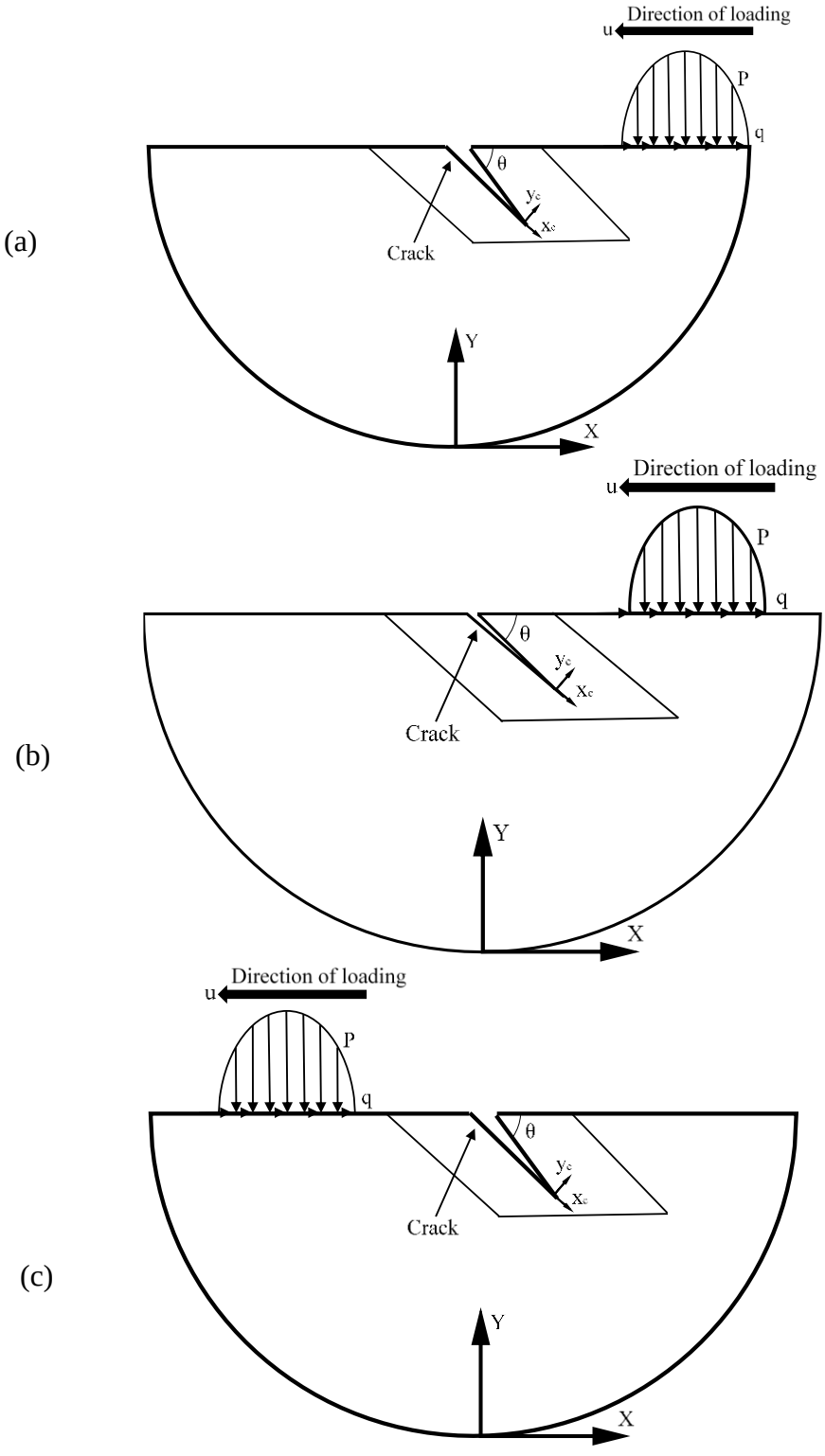


Figure 19: Crack mouth displacement with the direction of load.

| Case No | Friction Coefficient | Crack length, a (μm) | Inclination, θ° |
|---|---|---|---|
| 1 | 0 | 10 | 15 |
| 2 | | | 30 |
| 3 | | 20 | 15 |
| 4 | | | 30 |
| 5 | 0.1 | 10 | 15 |
| 6 | | | 30 |
| 7 | | 20 | 15 |
| 8 | | | 30 |
| 9 | 0.3 | 10 | 15 |
| 10 | | | 30 |
| 11 | | 20 | 15 |
| 12 | | | 30 |

Table 3: Simulation matrix for surface friction effect under the Hertzian loading condition.

| Case No | Type of Loading | Crack length, a (μm) | Inclination, θ° |
|---|---|---|---|
| 1 | Hertzian | 10 | 15 |
| 2 | | | 30 |
| 3 | | 20 | 15 |
| 4 | | | 30 |
| 5 | Sinusoidal | 10 | 15 |
| 6 | | | 30 |
| 7 | | 20 | 15 |
| 8 | | | 30 |

Table 4: Simulation matrix for loading effect.

The surface friction effect under the Hertzian pressure distribution are compared according to the simulation matrix as shown in Table 3. The total of twelve cases include the variation of the crack length as well as the crack orientation. The Hertzian contact is defined by the half width of $b = 10$ μm, and the maximum Hertzian pressure of $p_{\max} = 1$ MPa. The surface friction coefficients are selected as 0, 0.1 and 0.3, representing the conditions of friction free, low friction and high friction, respectively. For all the cases the friction coefficient between the crack faces is set at 0.1.

Considering the 10 μm crack length, the tensile mode I stress intensity factor, $K_I$ , behavior under the Hertzian pressure distribution is compared between different surface friction coefficients (0, 0.1 and 0.3) for different crack inclinations (15° and 30°) in Figure 20 (a) and (b). A similar comparison concerning the shear mode II stress intensity factor, $K_{II}$ , behavior is carried out in Figure 21 (a) and (b). Maintaining the other contact parameters while increasing the crack length from 10 μm to 20 μm, the same types of comparisons are performed in Figure 22 (a) and (b) for $K_I$ , and Figure 23 (a) and (b) for $K_{II}$ . It is observed, the increase in the crack orientation angle reduces the ranges of both the mode I and mode II SIFs. That explains why the surface initiated cracks commonly have a shallow inclination angle. Secondly, it is seen the increase of the surface friction leads to the reduction of the $K_I$ amplitude when the crack inclination angle is shallow, i.e. 15°. The underlying mechanism is the competition between the impacts of the normal pressure and the tangential shear on the stress concentration in the vicinity of the crack tip. The normal pressure that is compressive tends to close the crack, while the surface tangential shear as shown in Figure 19 points to the right and tries to open the crack.

Therefore, as the surface friction coefficient increases, the increased surface shear counteracts the normal pressure to alleviate the mode I stress intensity. As for the mode II SIF, it is observed to follow the same behavior as the surface friction increases for both the 15° and 30° crack orientations. It is interesting to find that the relationship between $K_I$ and the surface friction coefficient under the 30° inclination angle is different from that under the 15° angle. The mode I SIF is seen to first decrease and then increase as the friction coefficient increases.

The tensile mode I $K_I$ is compared between different crack lengths (10 μm and 20 μm) under various surface rolling friction coefficients (0, 0.1 and 0.3) for the 15° crack inclination angle considering the Hertzian pressure distribution in Figure 24. It is seen the increased crack length leads to the increased stress intensity factor for all surface friction conditions. The shear mode II $K_{II}$ is found to follow the same behavior as shown in Figure 25. Maintaining the other contact parameters, while increasing the crack inclination angle from 15° to 30°, the similar comparisons are performed for the tensile mode I $K_I$ and the shear mode II $K_{II}$ in Figure 26 and Figure 27, respectively. The same conclusion can be drawn from these figures.

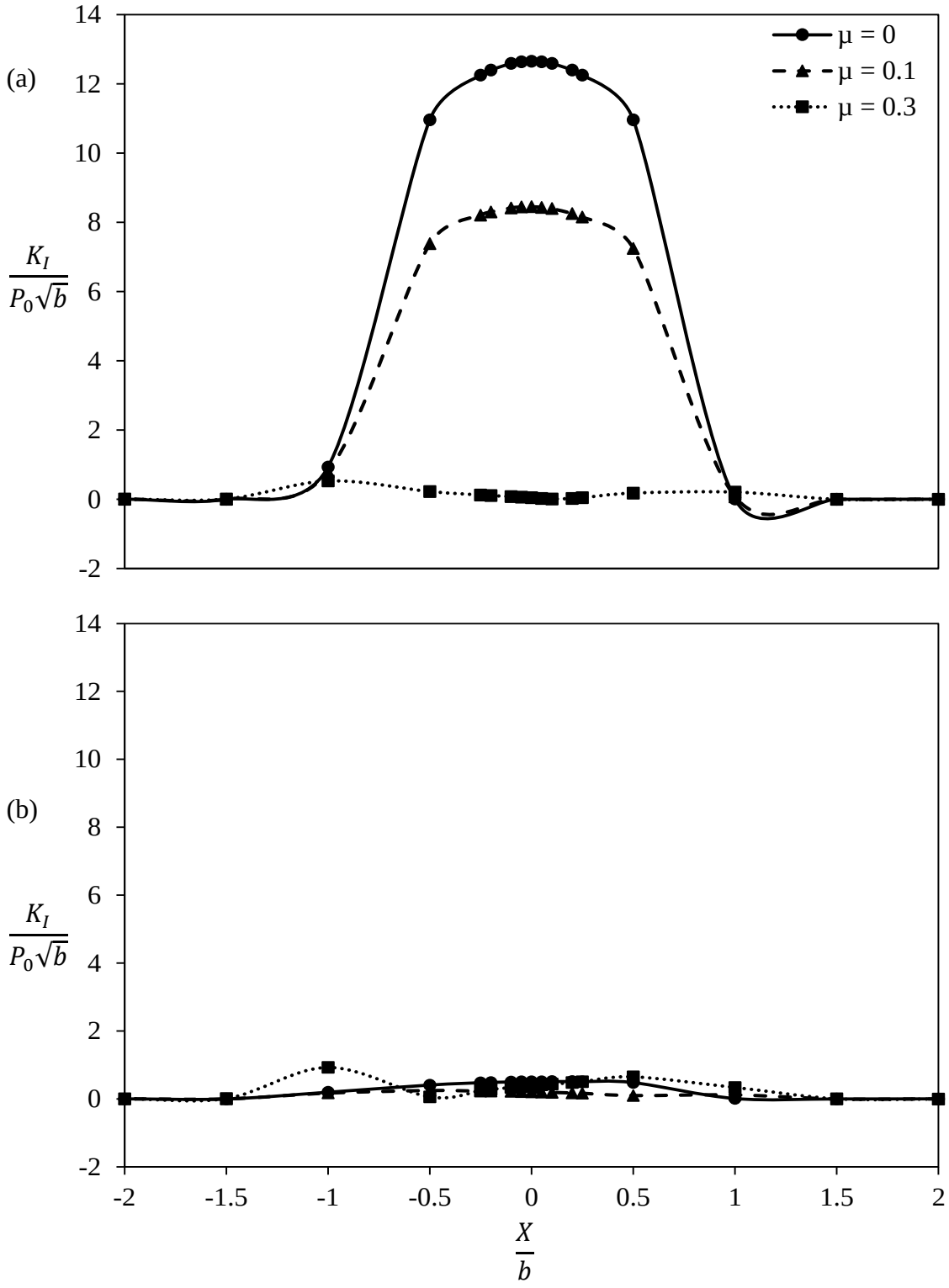


Figure 20: (a) $K_I$ at 15° crack inclination (b) $K_I$ at 30° crack inclination for 10 μm crack length under Hertzian pressure distribution.

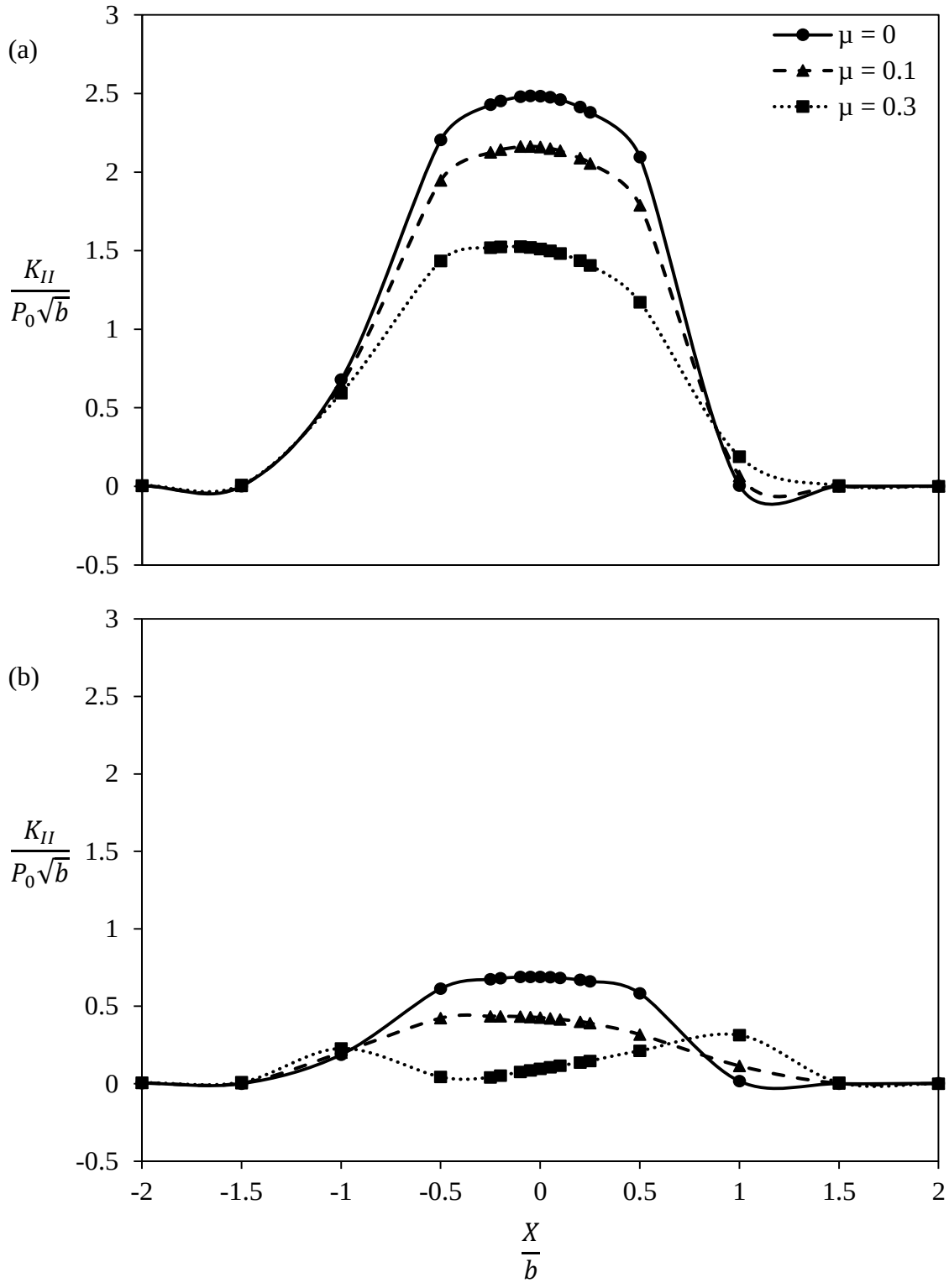


Figure 21: (a) $K_{II}$ at 15° crack inclination (b) $K_{II}$ at 30° crack inclination for 10 μm crack length under Hertzian pressure distribution.

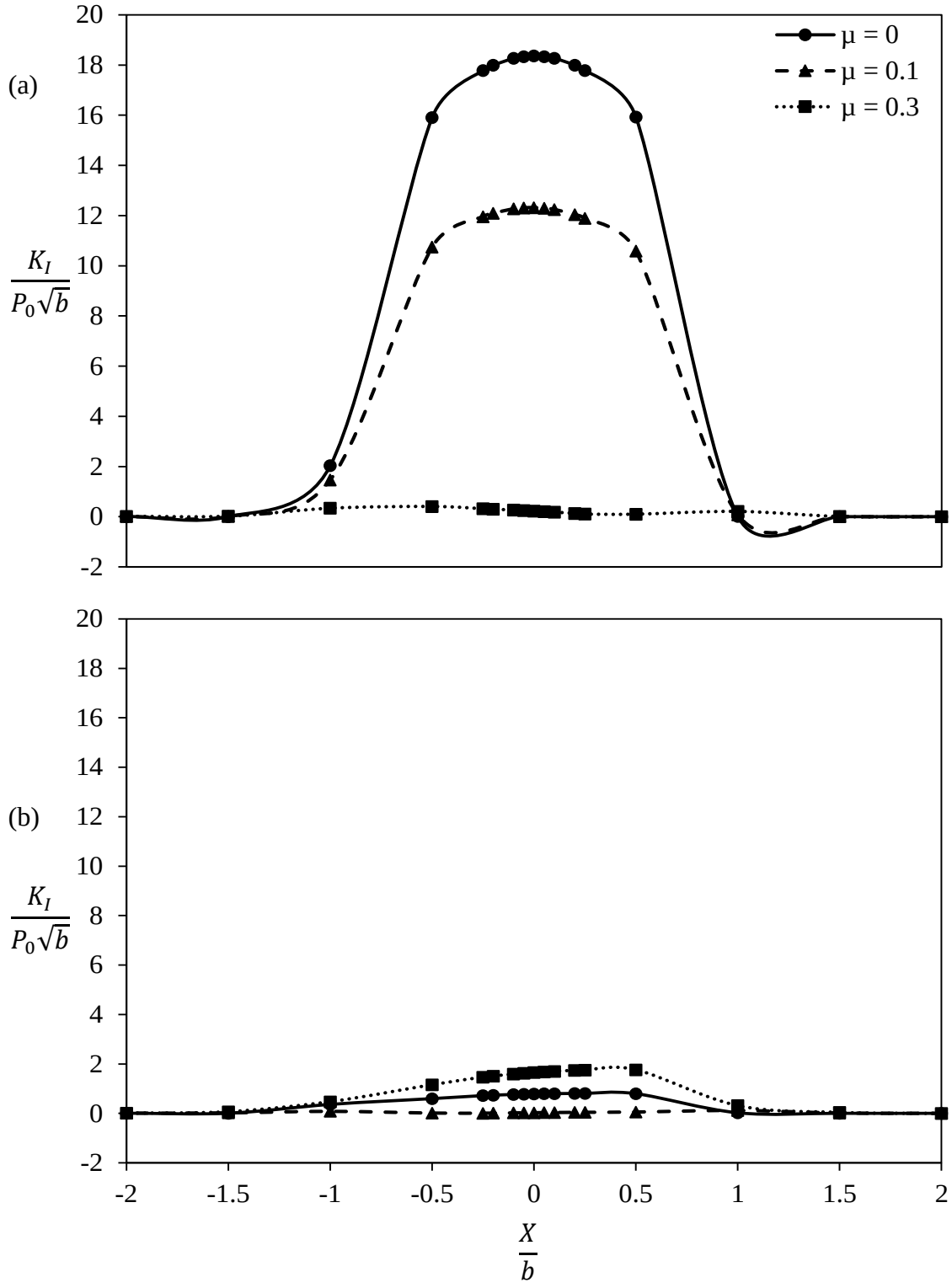


Figure 22: (a) $K_I$ at 15° crack inclination (b) $K_I$ at 30° crack inclination for 20 μm crack length under Hertzian pressure distribution.

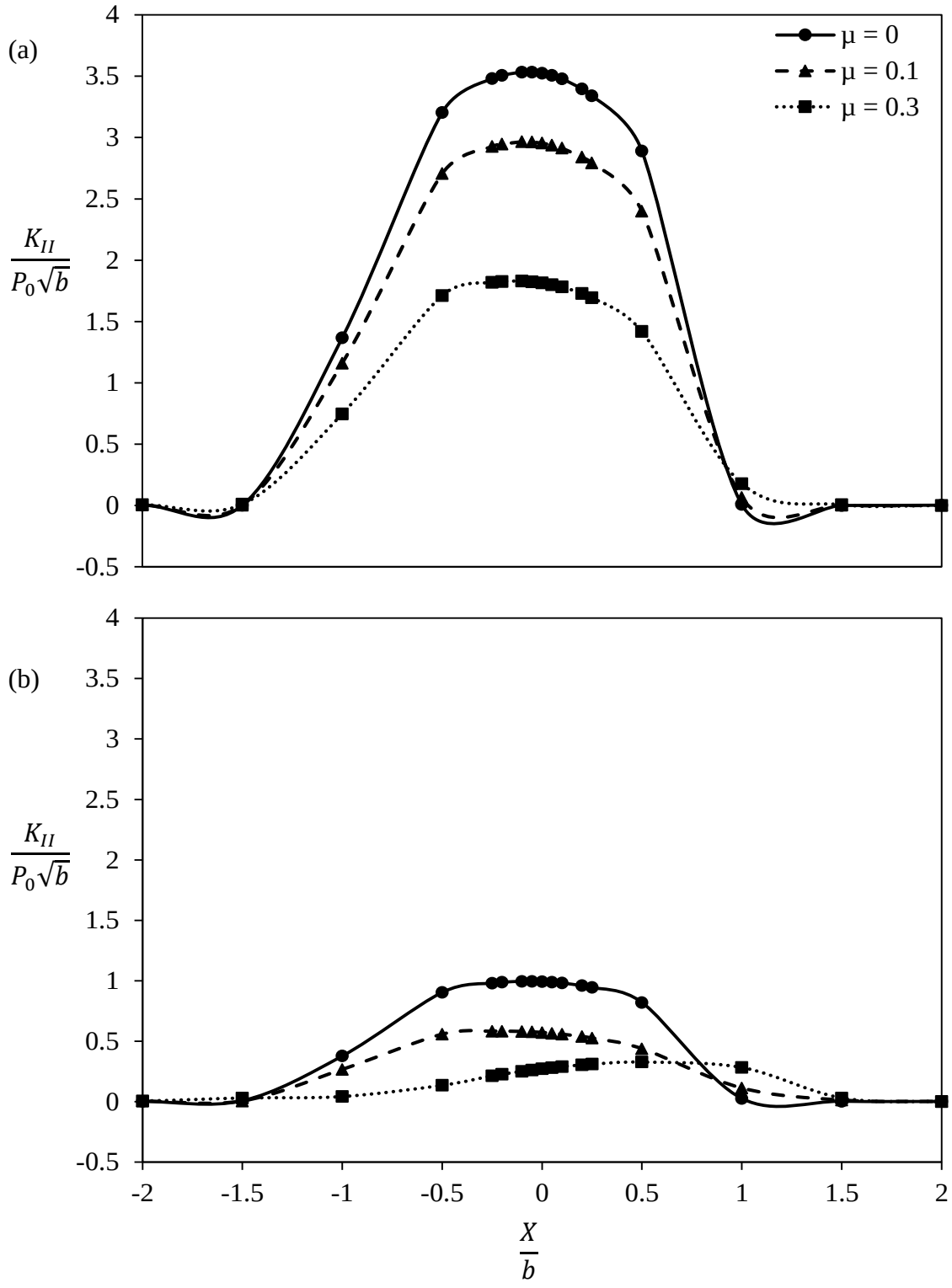


Figure 23: (a) $K_{II}$ at 15° crack inclination (b) $K_{II}$ at 30° crack inclination for 20 μm crack length under Hertzian pressure distribution.

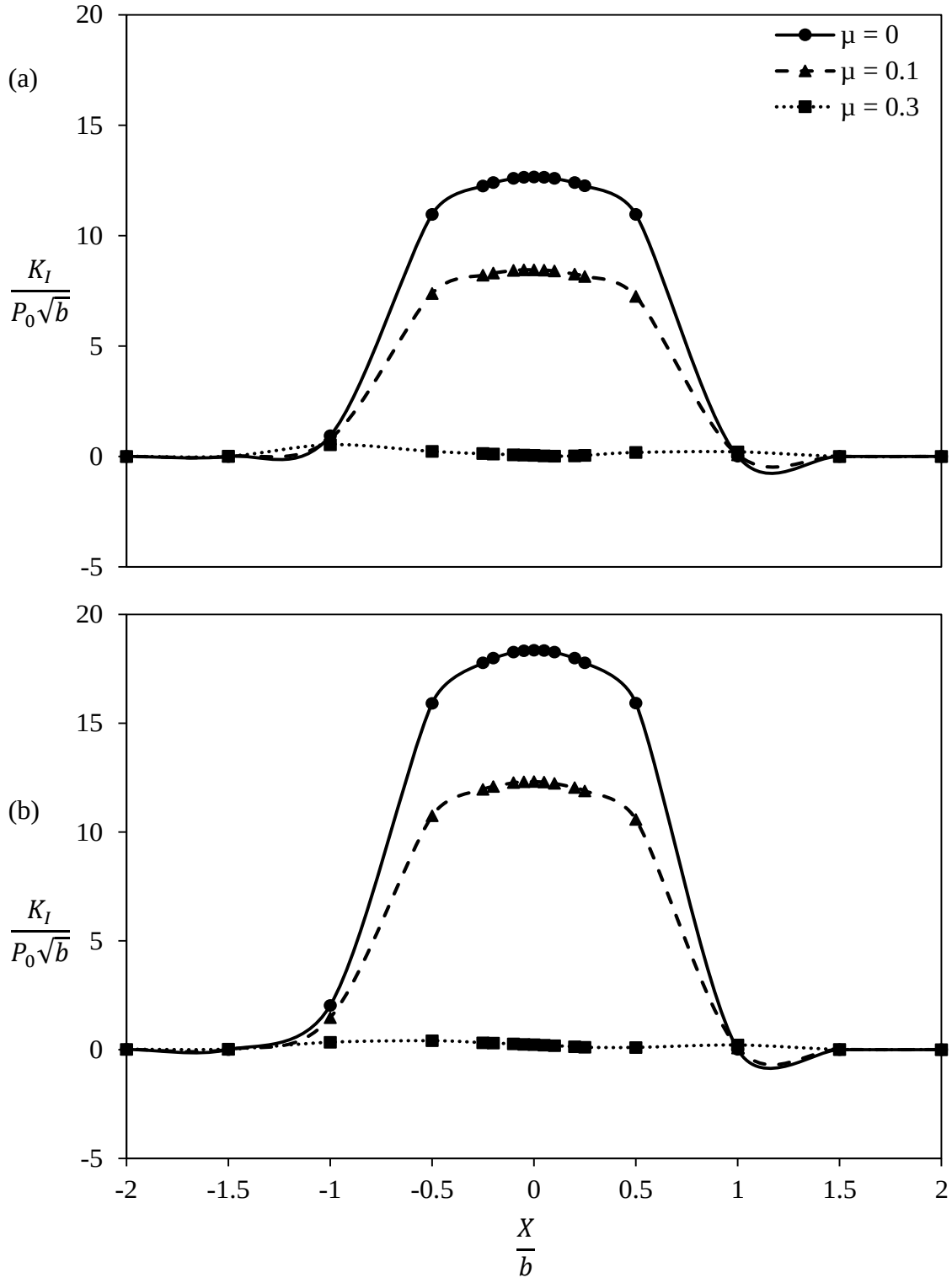


Figure 24: (a) $K_I$ at 10 μm crack length (b) $K_I$ at 20 μm crack length for 15° crack inclination under Hertzian pressure distribution.

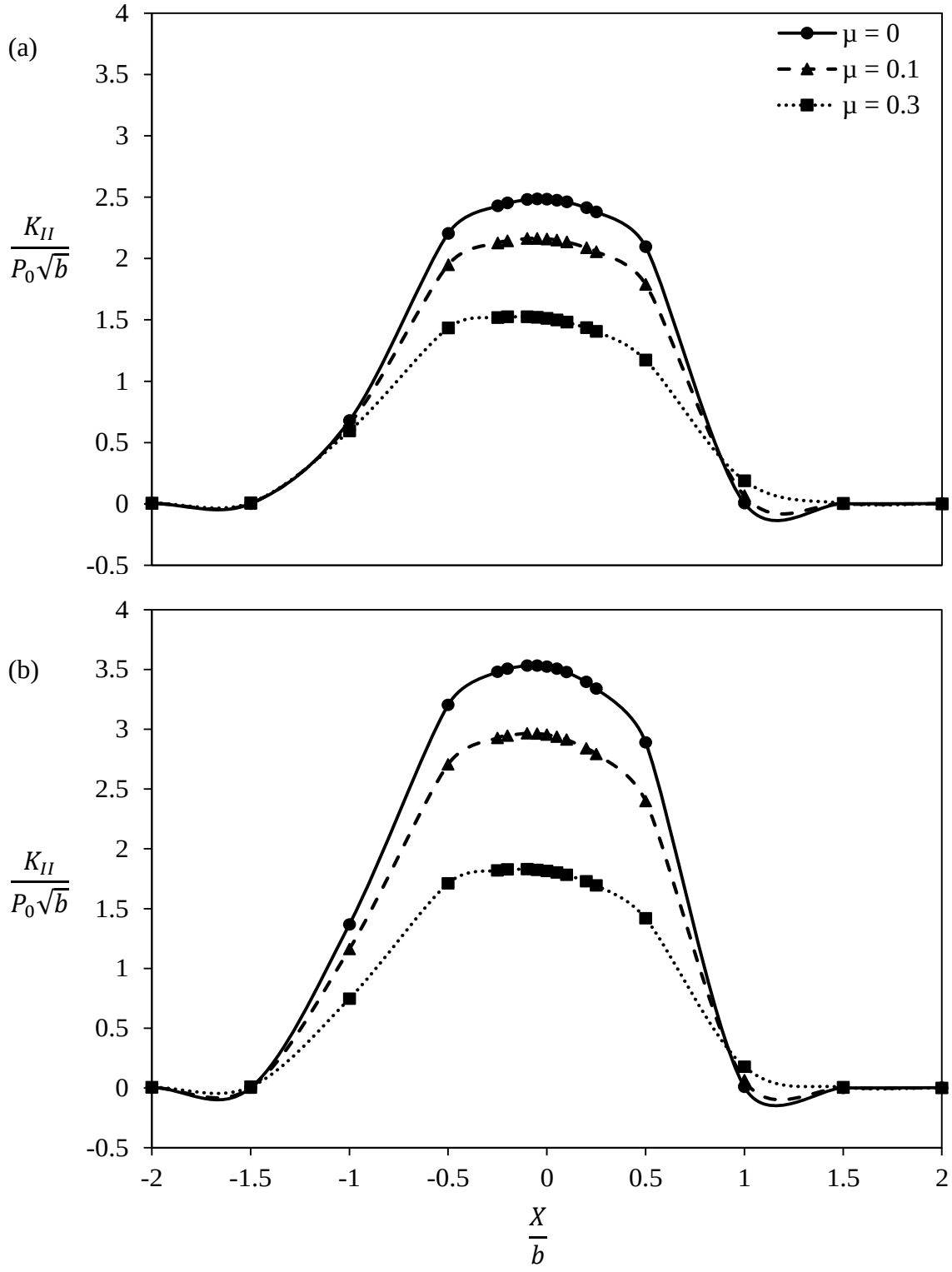


Figure 25: (a) $K_{II}$ at 10 μm crack length (b) $K_{II}$ at 20 μm crack length for 15° crack inclination under Hertzian pressure distribution.

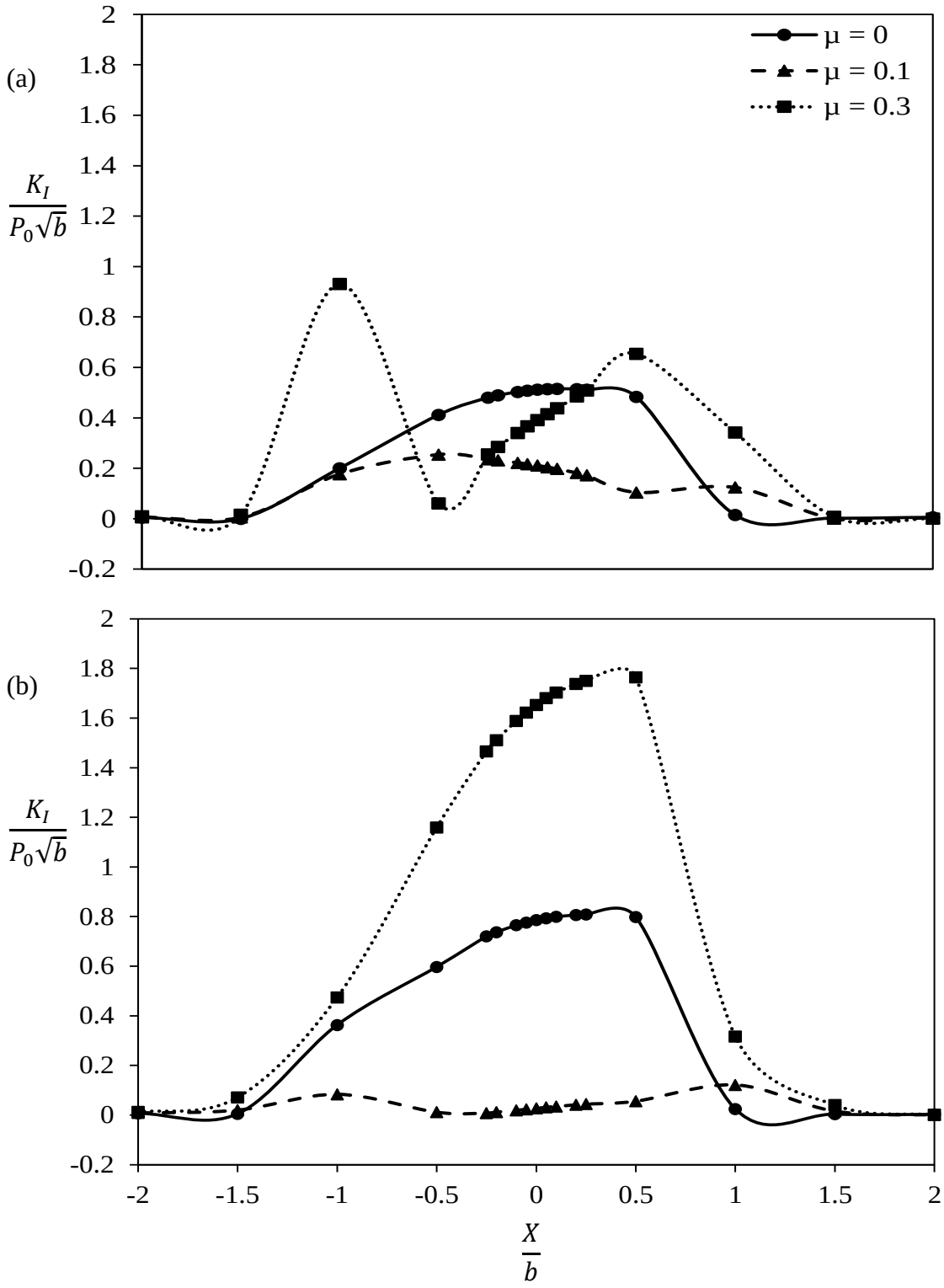


Figure 26: (a) $K_I$ at 10 μm crack length (b) $K_I$ at 20 μm crack length for 30° crack inclination under Hertzian pressure distribution.

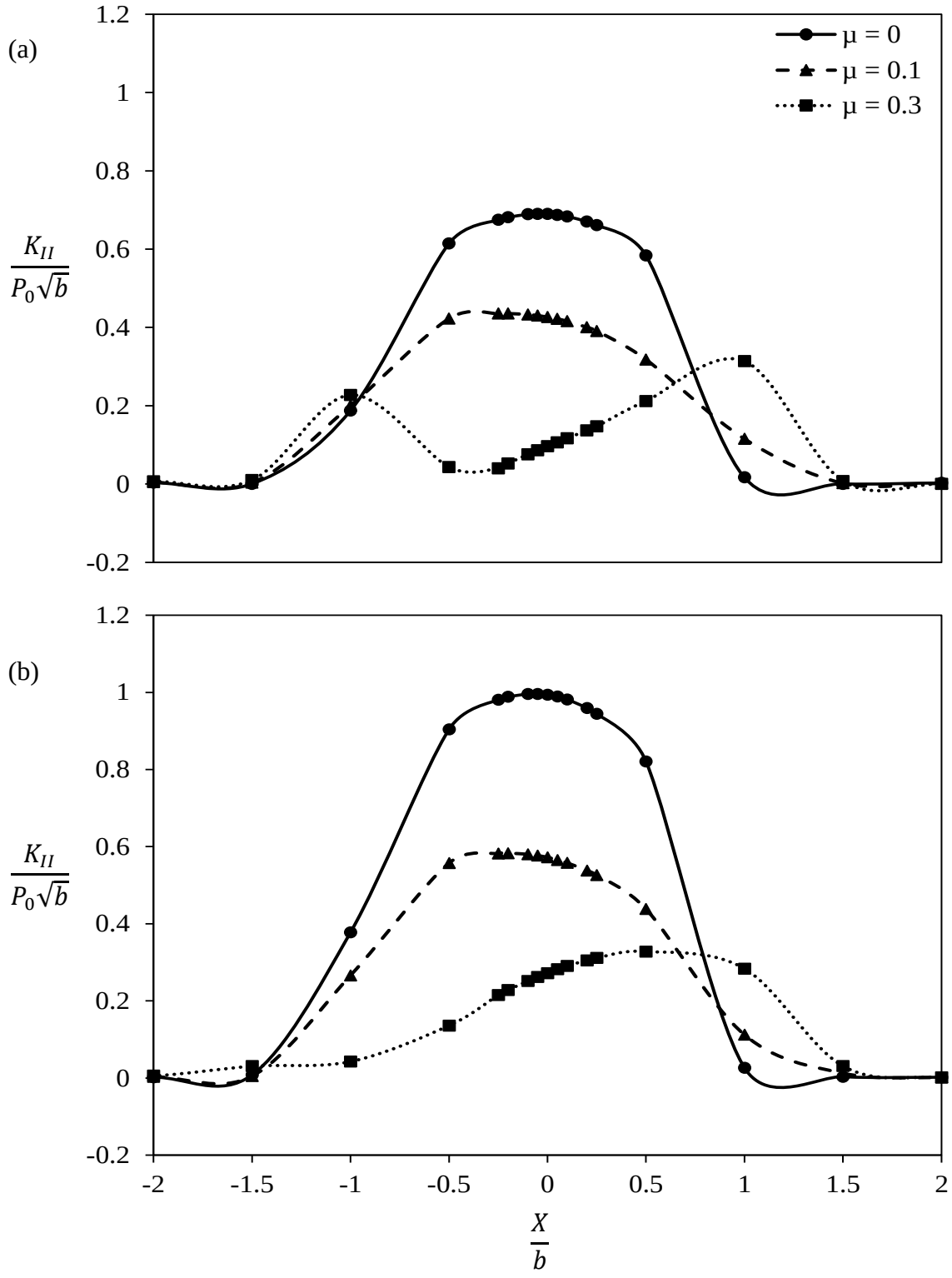


Figure 27: (a) $K_{II}$ at 10 μm crack length (b) $K_{II}$ at 20 μm crack length for 30° crack inclination under Hertzian pressure distribution.

The loading effects of the Hertzian and Sinusoidal pressure distribution on the stress intensity factors are compared according to the simulation matrix as shown in Table 4. For all the cases considered, the constant half width of the loading zone, $b = 10\,\mu\text{m}$, the maximum pressure of the distribution, $p_{\max} = 1\,\text{MPa}$ and the friction coefficient between the crack faces of $\mu = 0.1$ are employed. In these simulations, the surface friction is excluded.

The $K_I$ SIF induced by the Hertzian pressure distribution and the Sinusoidal pressure distribution is compared in Figure 28 for both the 15° and 30° crack inclination angles, considering the 10 μm crack length. It is observed that both the location and magnitude of the maximum $K_I$ are altered when the Hertzian pressure is replaced with the Sinusoidal one. For instance, the normalized $K_I$ range is reduced from 12.7 to 8.9, recording a 30% reduction for the shallow crack inclination angle of 15°. Again, the larger crack inclination angle is shown to results in smaller SIF. A similar comparison for the $K_{II}$ SIF is carried out in Figure 29 and the same conclusion can be drawn. While keeping the other contact parameters the same and increasing the crack length from 10 μm to 20 μm, the behavior of $K_I$ and $K_{II}$ are compared between the Hertzian and Sinusoidal loading conditions in Figure 30 and Figure 31, respectively. The impact of the different loading conditions on the stress intensity factors are observed to be very similar to those in Figure 28 and Figure 29.

The next comparison is to examine the crack length effect under the Sinusoidal loading condition. Figure 32 (a) and (b) show the comparison of $K_I$ between the 10 μm and 20 μm crack length for the 15° and the 30° crack inclination angles, respectively. The

same type of comparison for $K_{II}$ is performed in Figure 33 (a) and (b). It is seen when the crack orientation is shallow, i.e. 15° inclination angle, the larger crack length leads to the smaller range for both the $K_I$ and $K_{II}$ ranges. However, under the larger crack inclination angle of 30°, this trend is reversed, i.e. the smaller crack length corresponds to the smaller SIF ranges. The last comparison that concerns the crack inclination angle impact on the SIFs is carried out in Figure 34 (a) and (b) for $K_I$, and in Figure 35 (a) and (b) for $K_{II}$. It is observed for the short crack length of 10 μm, both the $K_I$ and $K_{II}$ ranges decrease as the crack inclination angle increases. This relationship is reversed when the crack length is increased to 20 μm.

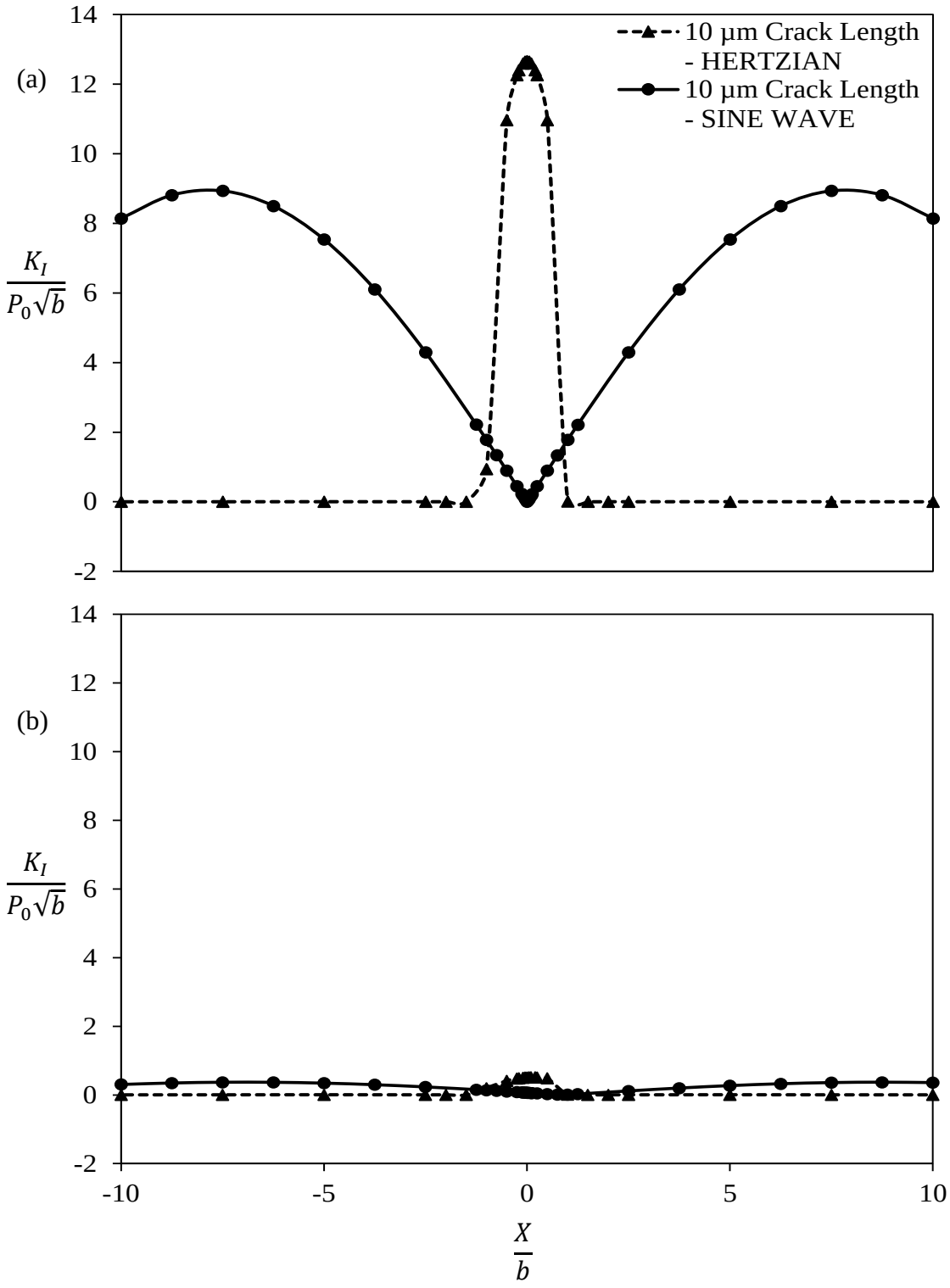


Figure 28: (a) $K_I$ at 15° crack angle (b) $K_I$ at 30° crack angle for 10 µm under both Hertzian and Sinusoidal pressure distribution.

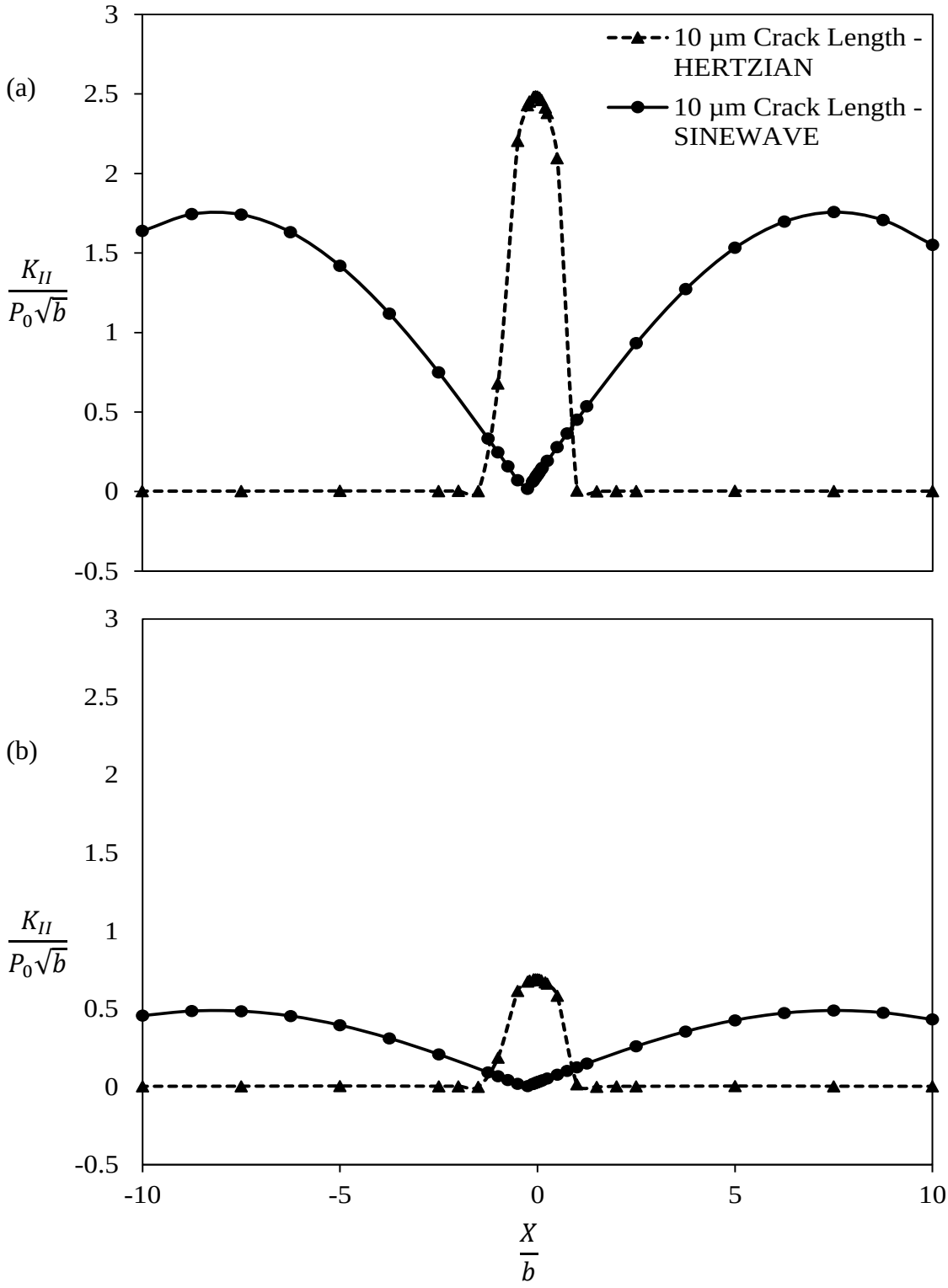


Figure 29: (a) $K_{II}$ at 15° crack angle (b) $K_{II}$ at 30° crack angle for 10 µm under both Hertzian and Sinusoidal pressure distribution.

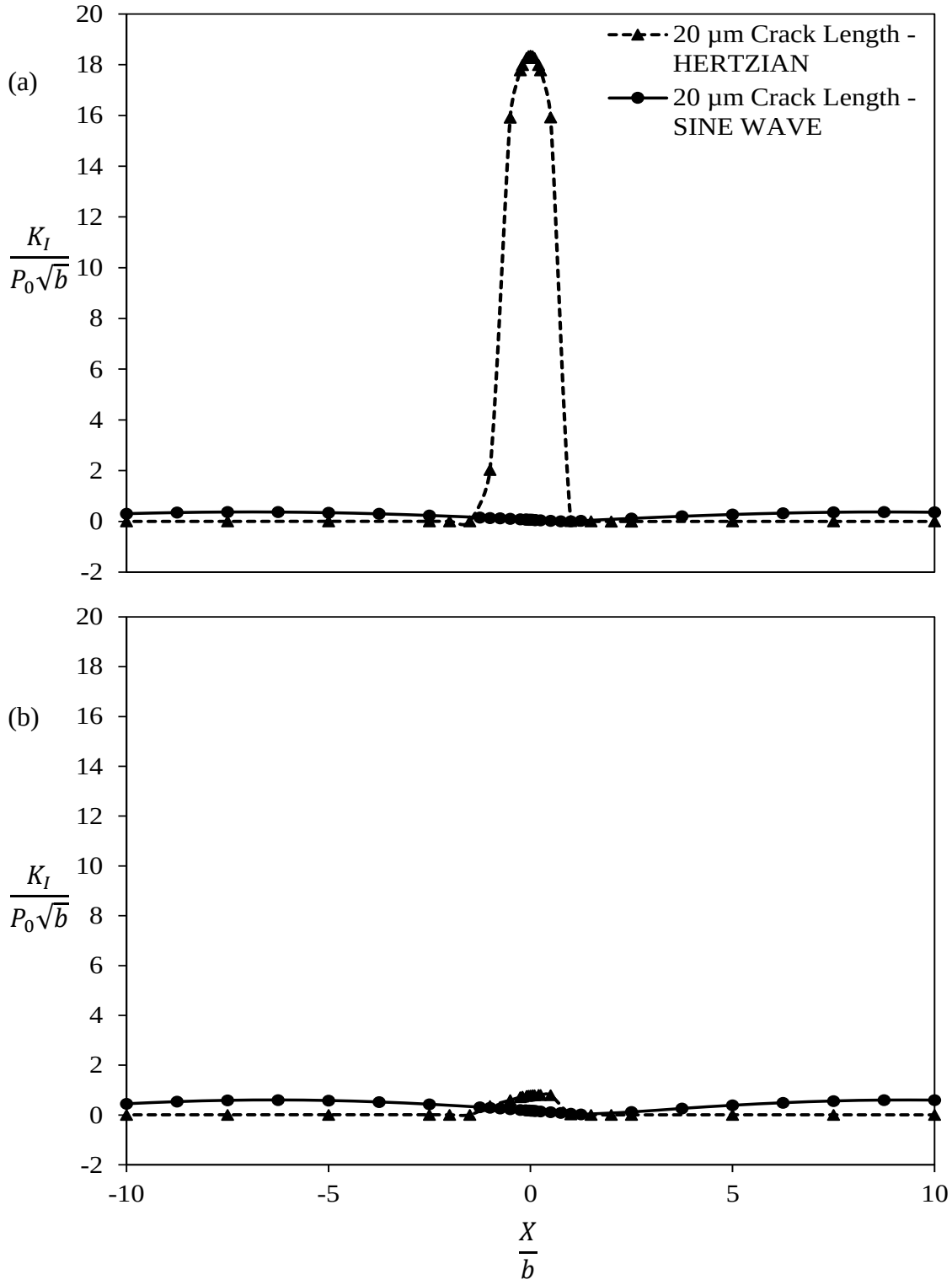


Figure 30: (a) $K_I$ at 15° crack angle (b) $K_I$ at 30° crack angle for 20 µm under both Hertzian and Sinusoidal pressure distribution.

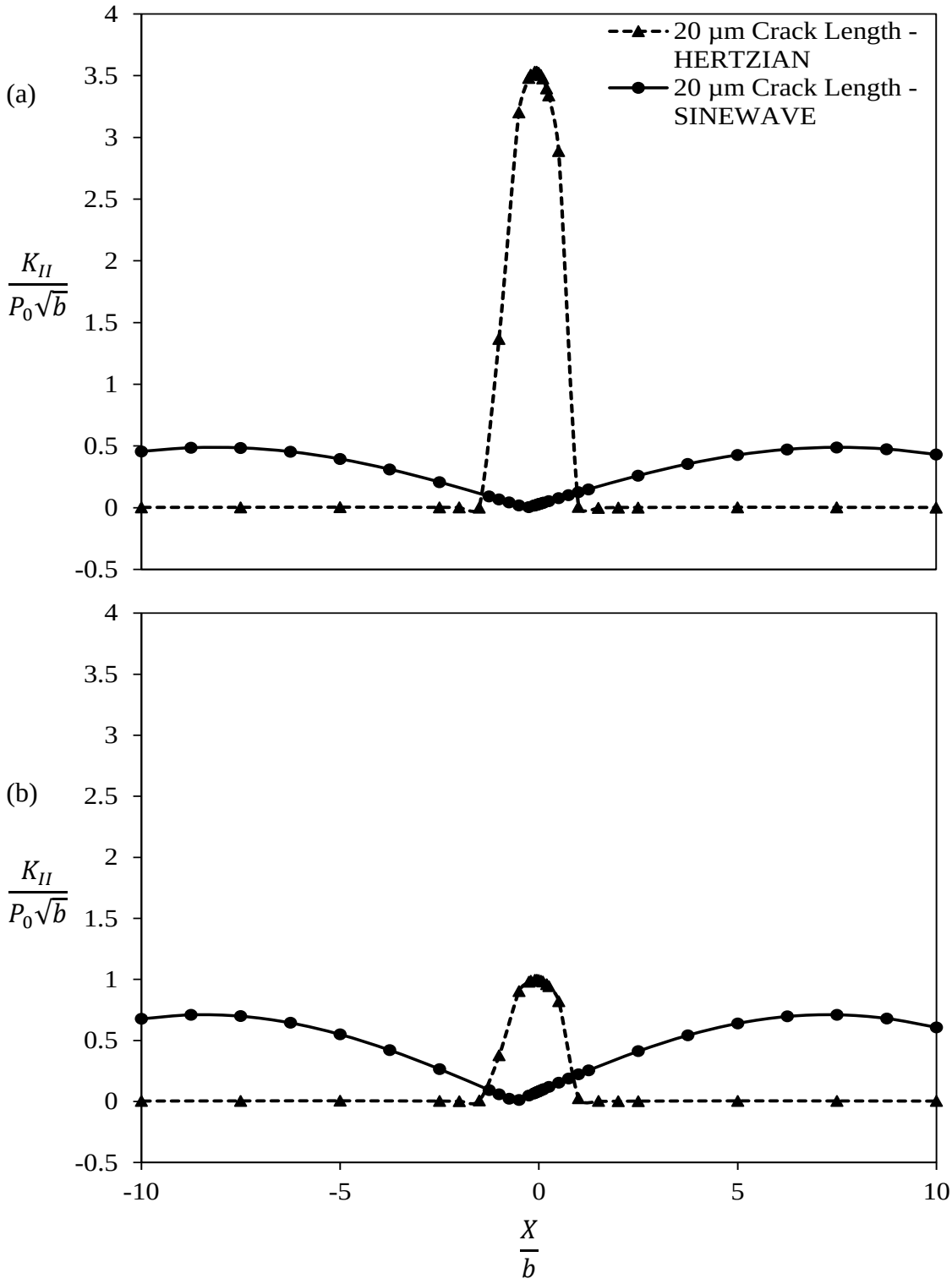


Figure 31: (a) $K_{II}$ at 15° crack angle (b) $K_{II}$ at 30° crack angle for 20 µm under both Hertzian and Sinusoidal pressure distribution.

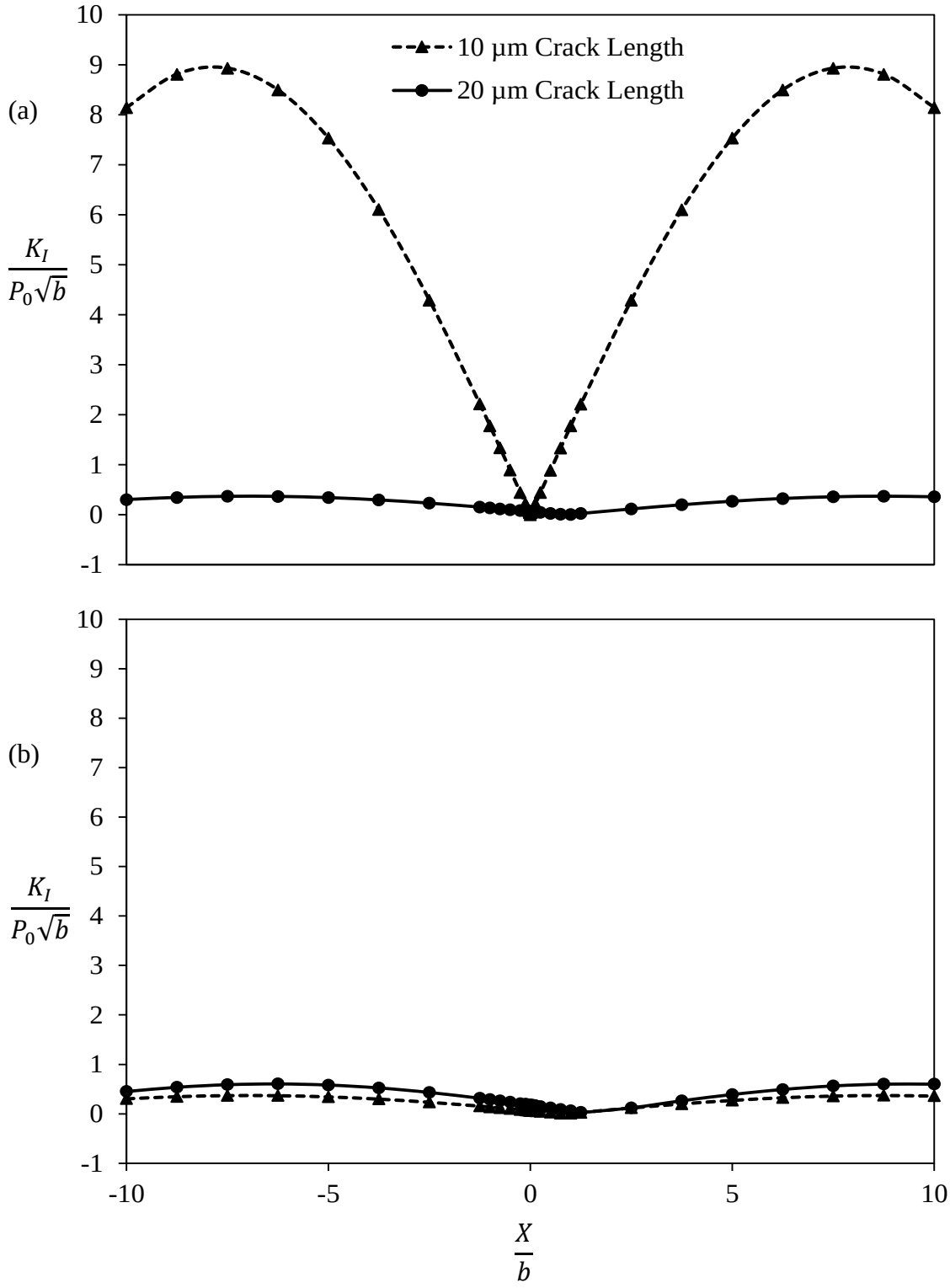


Figure 32: (a) $K_I$ for 15° crack angle (b) $K_I$ for 30° crack angle under Sinusoidal pressure distribution.

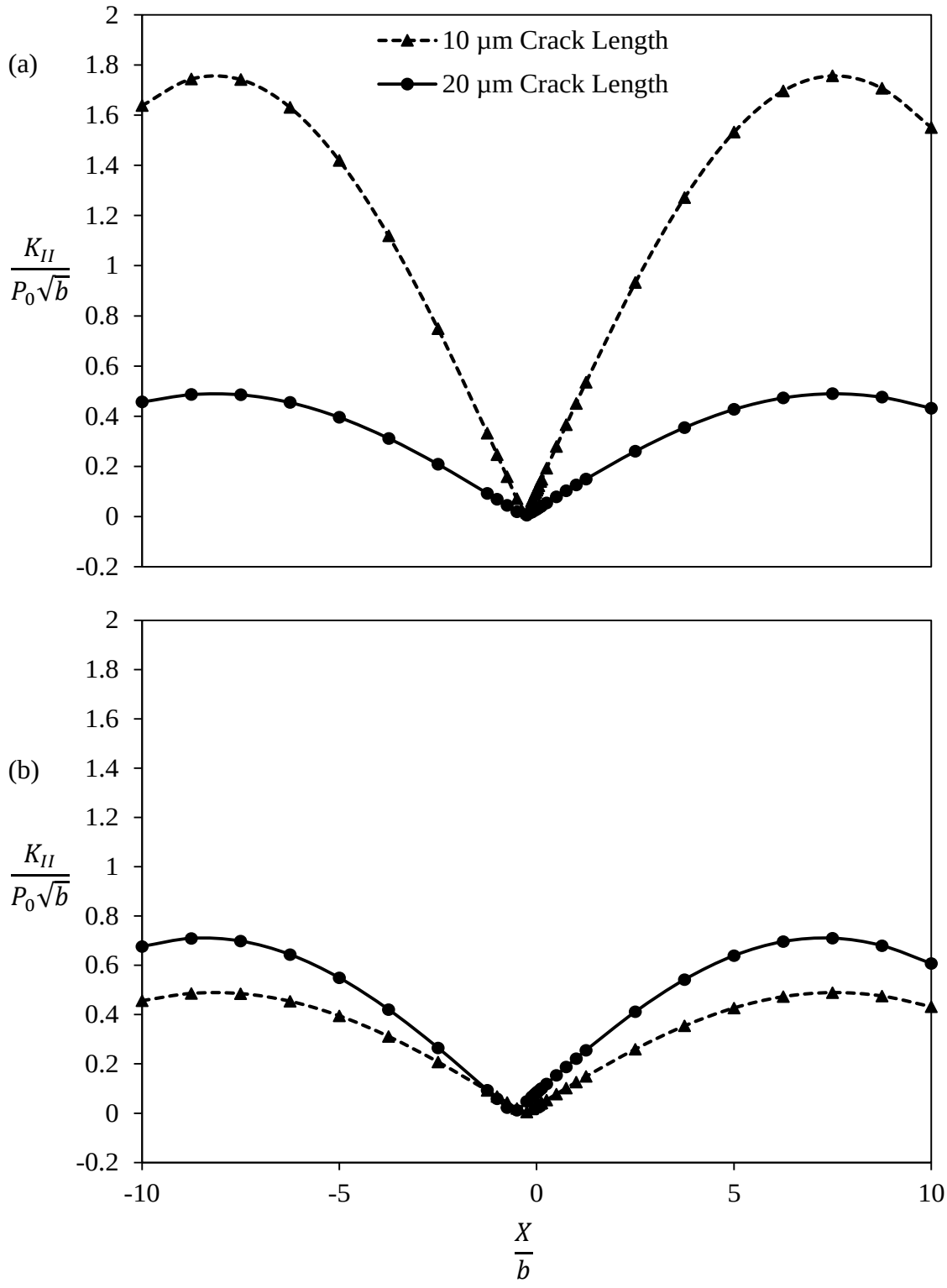


Figure 33: (a) $K_{II}$ for 15° crack angle (b) $K_{II}$ for 30° crack angle under Sinusoidal pressure distribution.

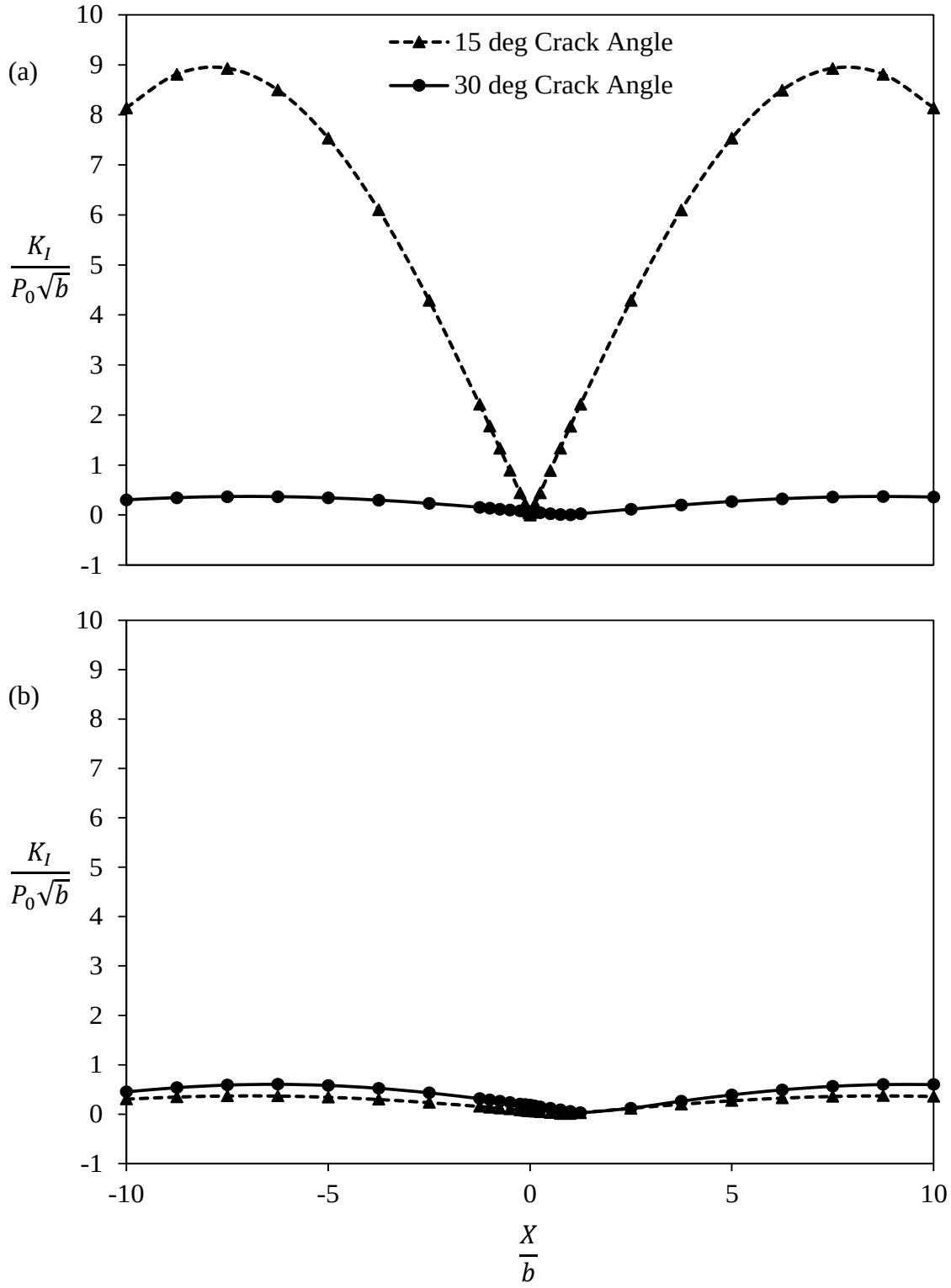


Figure 34: (a) $K_I$ for 10 μm crack length (b) $K_I$ for 20 μm crack length under Sinusoidal pressure distribution.

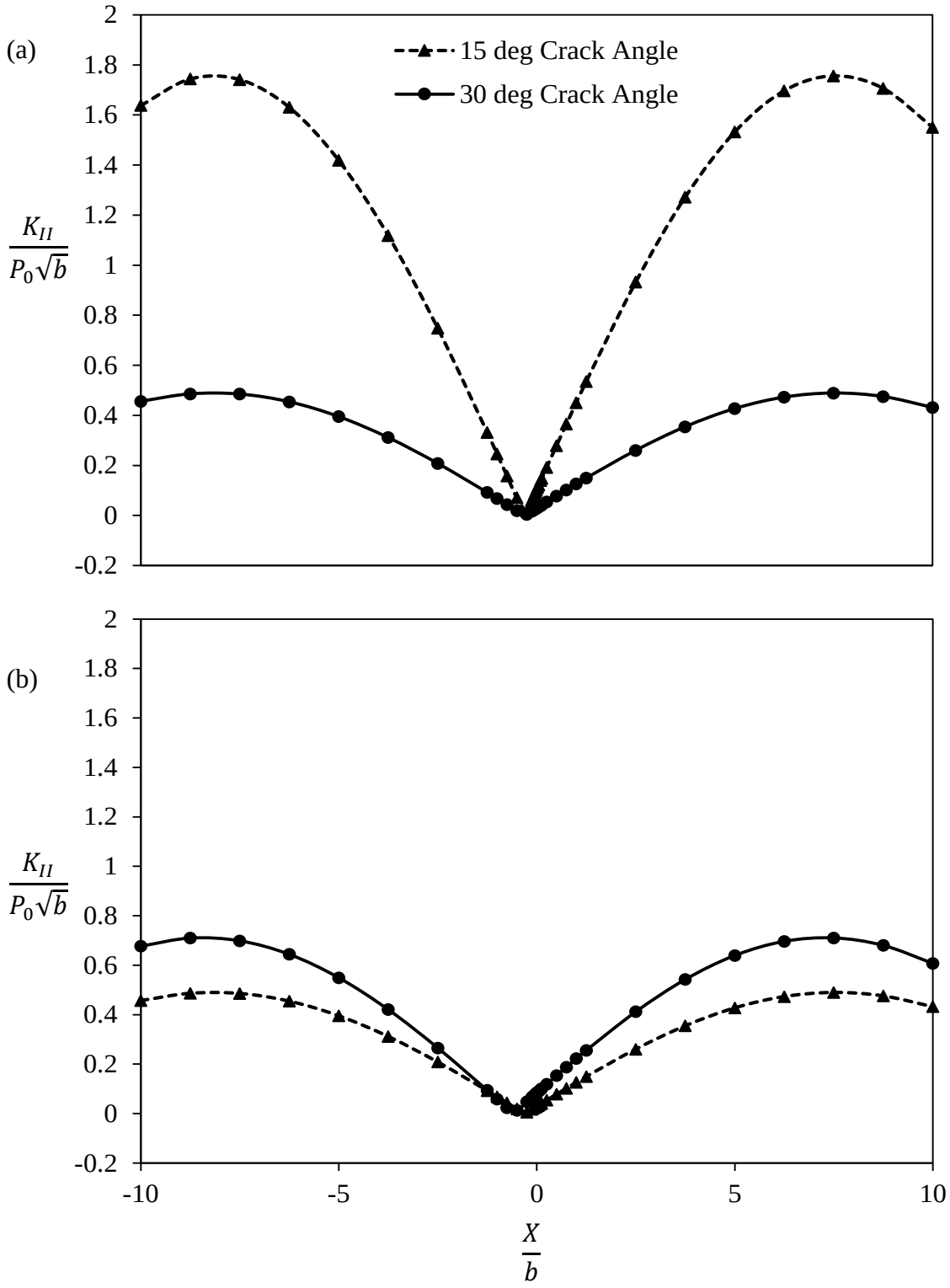


Figure 35: (a) $K_{II}$ for 10 μm crack length (b) $K_{II}$ for 20 μm crack length under Sinusoidal pressure distribution.

# CHAPTER 4

# SUMMARY AND CONCLUSIONS

## 4.1 Summary

This computational study investigated the impacts of the crack length, crack orientation, surface friction and loading condition on the surface nucleated micro-crack stress intensity factor behavior of a line contact problem, facilitating a better understanding of the micro-crack propagation behavior that is commonly observed in bearing and gear contacts. This work employed the finite element approach for the construction of the computational model. Owing to the facts that (i) the micro-crack requires an extremely fine mesh in order to capture the stress concentration around the crack tip accurately, and (ii) the contact body itself is large, a large number of finite elements is required for the discretization of the entire contact component, thus, imposing overwhelming computational efforts and unaffordable computational memory. To overcome this problem, a sophisticated new meshing scheme that is composed of a three-stage meshing was developed. This approach first constructs a fine mesh zone in the vicinity of the micro-crack, then implements a coarse mesh zone that is far away from the micro-crack. Lastly,

a transition zone is established in between the fine and coarse mesh zones to ensure a continuous and smooth element size transition. This meshing scheme discretize the entire contact component in an efficient manner, allowing the fast and accurate solution of the displacement and stress distributions.

For the quantification of both the mode I and mode II stress intensity factors, two levels of crack length (10 μm and 20 μm), two levels of crack inclination angle ($15^\circ$ and $30^\circ$), and three levels of contact surface friction coefficients (0, 0.1, and 0.3) are considered. These contact parameter variations yield a total of twelve simulation cases under the Hertzian pressure loading condition, where the maximum pressure is 1 MPa and the half Hertzian width is 100 μm. Besides this Hertzian loading condition that represent the pressure under the relatively smooth surfaces, a Sinusoidal pressure distribution was also implemented to imitate the loading condition when the surface is relatively rough. For all the simulations performed in this study, the friction coefficient at the crack face is set constant at 0.1, assuming the boundary lubrication condition.

## 4.2 Conclusions and Recommendations for Future Work

A total of twelve simulations were carried out under the Hertzian loading condition to investigate the impacts of the crack length, the crack inclination angle and the contact surface fiction coefficient on the ranges of the mode I and mode II stress intensity factors, which dictate the crack propagation behavior. Another set of simulations for the Sinusoidal loading condition was performed as well, however, excluding the surface friction effect.

The obtained ranges of the SIFs are summarized in Table 5 and Table 6 below. It can be concluded under the Hertzian loading condition that the increase in the crack orientation angle reduces the ranges of both the mode I and mode II SIFs, which explains why the surface initiated cracks commonly have a shallow inclination angle.

Secondly, it is seen the increase of the surface friction leads to the reduction of the $K_I$ amplitude when the crack inclination angle is shallow. The mode II SIF is observed to follow the same behavior as the surface friction increases. It was interesting to find that the relationship between $K_I$ and the surface friction coefficient under the 30° inclination angle is different from that under the 15° angle. The mode I SIF was seen to first decrease and then increase as the friction coefficient increases. As for the crack length effect, it is found that the increased crack length leads to the increased stress intensity factors. Under the Sinusoidal loading condition, these contact parameters showed different impact on the SIFs. It was shown, when the crack orientation is shallow, the larger crack length leads to the smaller range for both the $K_I$ and $K_{II}$ ranges. However, under the larger crack inclination angle, this trend was reversed. Concerning the inclination angle effect, it was found both the $K_I$ and $K_{II}$ ranges decreased as the crack inclination angle increased for a shorter crack. This relationship was reversed when the crack length became longer.

| Case No | Inclination, θ° | Crack length, a (μm) | Friction Coefficient | Crack length/half width, (a/b) | $\Delta K_I$ | $\Delta K_{II}$ |
|---|---|---|---|---|---|---|
| 1 | 15 | 10 | 0 | 0.1 | 1.27E+01 | 2.48E+00 |
| 2 | | | 0.1 | 0.1 | 8.45E+00 | 2.16E+00 |
| 3 | | | 0.3 | 0.1 | 5.33E-01 | 1.53E+00 |
| 4 | | 20 | 0 | 0.2 | 5.15E-01 | 6.90E-01 |
| 5 | | | 0.1 | 0.2 | 2.54E-01 | 4.35E-01 |
| 6 | | | 0.3 | 0.2 | 9.31E-01 | 3.14E-01 |
| 7 | 30 | 10 | 0 | 0.1 | 1.84E+01 | 3.53E+00 |
| 8 | | | 0.1 | 0.1 | 1.23E+01 | 2.97E+00 |
| 9 | | | 0.3 | 0.1 | 4.11E-01 | 1.83E+00 |
| 10 | | 20 | 0 | 0.2 | 8.08E-01 | 9.96E-01 |
| 11 | | | 0.1 | 0.2 | 1.22E-01 | 5.83E-01 |
| 12 | | | 0.3 | 0.2 | 1.76E+00 | 3.28E-01 |

Table 5: Stress Intensity Matrix for Hertzian loading under traction.

| Case No | Type of loading | Crack length, a (μm) | Inclination, θ° | Friction Coefficient | Crack length/ half width, (a/b) | $\Delta K_I$ | $\Delta K_{II}$ |
|---|---|---|---|---|---|---|---|
| 1 | Hertzian | 10 | 15 | 0 | 0.1 | 1.27E+01 | 2.48E+00 |
| 2 | | | 30 | 0.1 | 0.1 | 5.15E-01 | 6.90E-01 |
| 3 | | 20 | 15 | 0.3 | 0.2 | 1.84E+01 | 3.53E+00 |
| 4 | | | 30 | 0 | 0.2 | 8.08E-01 | 9.96E-01 |
| 5 | Sinusoidal | 10 | 15 | 0.1 | 0.05 | 8.93E+00 | 1.74E+00 |
| 6 | | | 30 | 0.3 | 0.05 | 3.64E-01 | 4.84E-01 |
| 7 | | 20 | 15 | 0 | 0.1 | 3.64E-01 | 4.84E-01 |
| 8 | | | 30 | 0.1 | 0.1 | 5.75E-01 | 6.98E-01 |

Table 6: Stress Intensity Matrix for Hertzian and Sinusoidal loading under no traction.

In further expand the research activity and elevate the understanding of the stress intensity behavior under the more practical operating condition, the following is recommended for the future work

- Improve the boundary condition definition along the crack face by introducing the locking, slipping and separation conditions.
- Increase the loading to be more representative of the automotive and aerospace gearing applications.
- Include the fluid trapping mechanism into the crack opening modeling.
- Investigate the friction direction effect on the stress intensity factor.

## REFERENCES


[1] Paris PC, Erdogan F. A critical analysis of crack propagation laws. Journal of Basic Engineering 1963; 85: 528–533.

[2] Li S, Kahraman A. A fatigue model for contacts under mixed elastohydrodynamic lubrication condition. International Journal of Fatigue 2011; 33: 427–436.

[3] Li S, Kahraman A, Klein M. A fatigue model for spur gear contacts operating under mixed elastohydrodynamic lubrication conditions. ASME Journal of Mechanical Design 2012; 134: 041007 (11 pages).

[4] Li, S., Kahraman, A. A physics-based model to predict micro-pitting lives of lubricated point contacts. International Journal of Fatigue 47, 205–215 (2013)

[5] Li S, Kahraman A. Micro-pitting fatigue lives of lubricated point contacts: Experiments and model validation. International Journal of Fatigue 2013; 48: 9–18.

[6] Li, S., Kahraman, A. A micro-pitting model for spur gear contacts. International Journal of Fatigue 59, 224–233 (2014)

[7] Li S. A computational study on the influence of surface roughness lay directionality on micropitting of lubricated point contacts. ASME Journal of Tribology 2015, 137(2), 021401 (10 pages).

[8] Li S. An investigation on the influence of misalignment on micro-pitting of a spur gear pair. Tribology Letters 2015, 60(3), 35 (12 pages).

[9] Li S, Wagner JJ. Determination of the accelerated RCF operating condition of the sun-planet contact of a tractor final drive using a computational method. Meccanica 2017; 52 (1): 431–440.

[10] Li S. A boundary element model for near surface contact stresses of rough surfaces. Computational Mechanics 2014; 54(3): 833–846.

[11] Li S, Anisetti A. A tribo-dynamic contact fatigue model for spur gear pairs. International Journal of Fatigue 2017; 98: 81–97.

[12] Miller GR, Keer LM, Cheng HS. On the mechanics of fatigue crack growth due to contact loading. Proc. R. Soc. Lond. A 1985; 397:197–209.

[13] Bower AF. The influence of crack face friction and trapped fluid on surface initiated rolling contact fatigue cracks. ASME Journal of Tribology 1988; 110:704–711.

[14] Bogdanski S. A rolling contact fatigue crack driven by squeeze fluid film. Fatigue & Fracture of Engineering Materials & Structures 2002; 25(11):1061–1071.

[15] Bogdanski S. Liquid-solid interaction at opening in rolling contact fatigue cracks. Wear 2005; 258:1273–1279.

[16] Bogdanski S, Trajer M. A dimensionless multi-size finite element model of a rolling contact fatigue crack. Wear 2005; 258:1265–1272.

[17] Balcombe R, Fowell MT, Olver AV, Ioannides S, Dini D. A coupled approach for rolling contact fatigue cracks in the hydrodynamic lubrication regime: The importance of fluid/solid interactions. Wear 2011; 271:720–733.

[18] Akama M, Mori T. Boundary element analysis of surface initiated rollng contact fatigue cracks in wheel/rail contact systems. Wear 2002; 253:35–41.

[19] Timoshenko SP, Goodier JN. Theory of elasticity, 3rd Edition, McGraw-Hill 1985, 923–935.

[20] Glodezˇ S, Winter H, Stuwe HP. A fracture mechanics model for the wear of gear flanks by pitting. Wear 1997; 208:177–83.

[21] Glodezˇ S, Flašker J, Ren Z. A new model for the numerical determination of pitting resistance of gear teeth flanks. Fatigue Fract Eng Mater Struct 1997; 20:71–83.

[22] Navarro A, Rios ER. Short and long fatigue crack growth – a unified model. Philosophical Magazine 1988; 57:15–36.

[23] Sun Z, Rios ER, Miller KJ. Modeling small fatigue cracks interacting with grain boundaries. Fatigue Fract. Eng. Meter 1991; 14:277–291.

[24] Hellen TK. On the methdod of virtual crack extensions. International Journal of Nuerical Methods Eng. 1975; 9:187–207.

[25] Flašker J, Fajdiga G, Glodezˇ S, Hellen TK. Numerical simulation of surface pitting due to contact loading. International journal of Fatigue 2001; 23:599–605.

[26] Fajdiga G, Sraml M. Fatigue crack initiation and propagation under cyclic contact loading. Engineering Fracture Mechanics 2009; 76:1320–1335.

[27] Kaneta M, Murakami Y. Propagation of semi-elliptical surface cracks in lubricated rolling/sliding elliptical contacts. ASME Journal of Tribology 1991; 113:270–275.

[28] Bogdanski S, Olzak M, Stupnicki J. Numerical stress analysis of rail rolling contact fatigue cracks. Wear 1996; 191:14–24.

[29] Bogdanski S, Brown MW. Modeling the three-dimensional behavior of shallow rolling contact fatigue cracks in rails. Wear 2002; 253:17–25.

[30] Way S. Pitting due to rolling contact. ASME Journal of Applied Mechanics 1935; 2:A49–A58.

[31] Dawson PH. The pitting of lubricated gear teeth and rollers. Power Transmission April and May 1961.

[32] Clayton P, Hill DN. Rolling contact fatigue of a rail steel. Proceedings of the 2nd International Symposium on Contact and Wear of Rail/Wheel Systems, Kingston, Rhode Island, 1986: 361–378.

[33] Nakajima A, Ichimaru K, Hirano F, Nishimura M. Effects of combination of rolling direction and sliding direction on pitting of rollers. JSLE International 1983:4:94–98.

[34] Evans HP, Snidle RW, Sharif KJ, Shaw BA, Zhang J. Analysis of micro-elastohydrodynamic lubrication and prediction of surface fatigue damage in micropitting tests on helical gears. ASME Journal of Tribology 2013:135:011501(9 pages).

[35] Horvath, Modelling of Crack Tip Singularity. TECHNISCHE MECHANIC, Band 14, Heft 2, (1994), 125-140, Manuskripteingang: 6, June 1994.

[36] Henshell, R.D.; Shaw, K. G.: Crack tip finite elements are unnecessary, Int. J. Num. Meth. Eng., 9, (1975), 495-507.

[37] Barsoum, R.S.: On the use of isoparametric finite elements in linear fracture mechanics, Int. J. Num. Meth. Eng., 10, (1976), 25-37.

[38] Barsoum, R. S.: Triangular quarter-point elements as elastic and perfectly plastic crack tip elements, Int. J. Num. Meth. Eng., 11, (1977), 85-98.

[39] Hussain, M. A.: Lorensen, W. E.; Pu, S. L.: The collased cubic isoparametric element as a singular element for crack problems, Int. J. Num. Meth. Eng., 12, (1978), 1727-1742.

[40] Ingraffea, A. R.; Lynn, P. P.: Transition elements to be used with quarter-point crack tip elements, Int. J. Num. Meth. Eng., 12, (1978), 1031-1036.

[41] ANSYS Elements Reference, Release 6.1, Swanson Analysis Systems, Inc., 2001.

[42] Dr. A.-V. Phan, ANSYS TUTORIAL – 2-D Fracture Analysis ANSYS Release 7.0, University of South Alabama